

QATAR UNIVERSITY

COLLEGE OF ARTS AND SCIENCES

CONSTRUCTION OF Fe_2O_3 /TRANSITION METAL DICHALCOGENIDES

HETEROSTRUCTURES FOR DYES PHOTODEGRADATION

BY

Aseel Yousef

A Thesis Submitted to
the College of Arts and Sciences
in Partial Fulfillment of the Requirements for the Degree of
Masters of Science in Material Science and Technology

June June 2023

© 2023. Aseel Yousef. All Rights Reserved.

COMMITTEE PAGE

The members of the Committee approve the Thesis of
Aseel Yousef defended on 30/05/2023.

Prof. Talal Altahtamouni
Thesis/Dissertation Supervisor

Dr. Abdul Shakoor
Committee Member

Prof. Aboubakr Abdullah
Committee Member

Dr. Dong Suk Han
Committee Member

Approved:

Ahmed Elzatahry, Dean, College of Arts and Sciences

ABSTRACT

YOUSEF, ASEEL, A., Masters : June : [2023], Material Science and Technology

Title: Construction of Fe₂O₃/Transition Metal Dichalcogenides Heterostructures for Dyes Photodegradation

Supervisor of Thesis: Talal, Altahtamouni.

Photocatalysis has been widely implemented in water purification due to its sustainability, high efficiency in degrading pollutants with low energy consumption, and it is economically and environmentally friendly. Hematite, also known as α -Fe₂O₃, is a promising photocatalyst due to its outstanding stability compared to other states of Fe₂O₃, non-toxicity, low cost, excellent antiferromagnetic properties, abundance in nature, corrosion resistance in acidic and alkaline media, recyclability, and the ability to harvest up to 40% of the solar spectrum. On the other hand, α -Fe₂O₃ shows several limitations including high electron-hole recombination rates, low conductivity, and small hole diffusion length. Forming heterostructures with Transition metal dichalcogenides (TMDs) helps in enhancing the performance of Fe₂O₃ by reducing the recombination rate and altering the transport rout.

In the past few decades, a plenty of research work was done on hematite to enhance its photocatalytic activity against water pollutants through several strategies including morphology control, doping and heterojunction formation. Indeed, constructing semiconductor heterojunctions has been considered to be one of the most effective methods as it provides the distinct properties of the combined elements and overcomes the limitations of each component. However, research work achieved on combining hematite with TMDs is still narrow. Thus, this study aims to accomplish an enhancement in the photocatalytic performance of Fe₂O₃ by constructing a heterostructure with a TMD material (WS₂). To the best of our knowledge, this is the first research work to prepare hematite nanorods heterostructured with a TMD material

synthesized via chemical vapor deposition (CVD) method. Furthermore, this hybrid system is optimized in this research in order to achieve an improved photodegradation activity against synthetic dyes such as Methylene Blue.

In this thesis, two reaction conditions of hematite synthesis were studied, which are precursors' ratio and annealing temperature, and they were found to affect the morphology of the hematite nanorods. Also, the distance between the tungsten source and the α -Fe₂O₃ sample (height) was found to influence the growth of WS₂ and the evolved photocatalytic activity of the obtained heterostructure which was examined against Methylene Blue dye solution under solar simulator irradiation. The best photodegradation performance was obtained by the heterostructure synthesized at a height of 6 mm with a degradation percentage of 64.9%, that is 3.4 and 2.8 times better than bare Fe₂O₃ and WS₂, respectively.

DEDICATION

This thesis is dedicated to whom I owe everything, my parents.

And to my soulmate & number one supporter, my husband.

ACKNOWLEDGMENTS

All praise and thanks to Allah for his endless blessings and guidance throughout my life journey.

I would like to express my sincere thanks to my supervisor, Prof. Talal Altahtamouni for providing precious advising during the research work. I acknowledge his efforts and I was honored to work and study under his supervision.

Also, sincere thanks to my thesis committee members, Prof. Aboubakr M. Abdullah, Dr. Abdul Shakoor, and Dr. Dong Suk Han as this work has benefited from their suggestions and comments.

I would like to thank the technical support from Central Laboratory Unit (CLU) and Center for Advanced Materials (CAM) at Qatar University.

Last but not least, I am very grateful for my beloved family, friends, and colleagues for their continuous support and encouragement.

TABLE OF CONTENTS

DEDICATION	v
ACKNOWLEDGMENTS	vi
LIST OF TABLES	ix
LIST OF FIGURES	x
CHAPTER 1: INTRODUCTION	1
1.1. Principle of Photocatalysis in Semiconductors.	1
1.2. Photocatalytic Dyes Degradation	2
1.3. Fe ₂ O ₃ as a Photocatalyst.....	3
1.3.1. Structure.....	3
1.3.3. Synthesis	6
1.4. WS ₂ as a Photocatalyst.....	7
1.4.1. Structure.....	7
1.4.2. Properties	8
1.4.3. Synthesis	9
CHAPTER 2: LITRATURE REVIEW	9
CHAPTER 3: EXPERIMENTAL METHODOLOGY	15
3.1. Materials Synthesis Methods	15
3.1.1. Hydrothermal Technique	15
3.1.2. Chemical Vapor Deposition (CVD)	16
3.2. Materials Characterization Techniques	17
3.2.1. X-Ray Diffraction.....	17

3.2.2. Raman Spectroscopy	18
3.2.3. Scanning Electron Microscopy (SEM).....	19
3.2.4. X-ray Photoelectron Spectroscopy (XPS)	21
CHAPTER 4: RESULTS AND DISCUSSION.....	21
4.1 Synthesis of Fe ₂ O ₃	21
4.1.1. Materials	21
4.1.2. Fe ₂ O ₃ NRs synthesis method.....	21
4.1.3. Photodegradation of Methylene Blue	25
4.2. Construction of WS ₂ /Fe ₂ O ₃ Heterostructures	26
4.2.1. Materials	26
4.2.2. Preparation of WS ₂ / Fe ₂ O ₃ Heterostructures	27
4.2.3. Proposed Photocatalytic Mechanism.....	36
FUTURE PRESPECTIVE	38
REFERENCES	39

LIST OF TABLES

Table 1. Crystal structures of three types of Fe_2O_3 ($\alpha\text{-Fe}_2\text{O}_3$, $\gamma\text{-Fe}_2\text{O}_3$, and $\varepsilon\text{-Fe}_2\text{O}_3$) (39).	5
Table 2. Different techniques for MB dye degradation from wastewater in recent studies.	14

LIST OF FIGURES

Figure 1. Schematic clarification of the photocatalytic process on a semiconductor (19).	2
Figure 2. 2H-MX ₂ and 1T-MX ₂ unit cell structures (70).	8
Figure 3. Schematic of the proposed photocatalytic mechanism of the photocatalyst Fe ₂ O ₃ /WS ₂ (97).	11
Figure 4. The setup used for hydrothermal method.	16
Figure 5. The used CVD system.	17
Figure 6. Schematic explanation of Bragg's Law (114).	18
Figure 7. Schematic illustration of the scattering types in the Raman spectroscopy (118).	19
Figure 8. Schematic of various primary electron beam interactions with the specimen (120).	20
Figure 9. SEM images of top view (a) and cross section (b) of as-prepared α -Fe ₂ O ₃ NRs.	22
Figure 10. Raman spectrum (a) and XRD pattern (b) of Fe ₂ O ₃ NRs.	23
Figure 11. Surface SEM images of different precursors ratios of NaNO ₃ : FeCl ₃	24
Figure 12. Surface SEM images of hematite NRs annealed at three different temperatures.	25
Figure 13. The used experimental setup for the photodegradation of MB by the prepared photocatalysts.	26
Figure 14. Schematic of the used experimental setup in CVD.	28
Figure 15. SEM surface images of WS ₂ /Fe ₂ O ₃ heterostructures constructed at 4 different heights.	29
Figure 16. Raman spectrum (a) and XRD pattern (b) of WS ₂ /Fe ₂ O ₃ heterostructure.	30
Figure 17. XPS spectra of the heterostructure WS ₂ /Fe ₂ O ₃ (a), W 4f (b), S 2p (c), Fe 2p	

(d), and O 1s (e).	32
Figure 18. MB dye absorption spectra at several time intervals using Fe ₂ O ₃ sample (a), WS ₂ sample (b), and the heterostructure sample WS ₂ /Fe ₂ O ₃ (c).....	33
Figure 19. Photodegradation efficiency plots (a) and the kinetics plots (b) of the as-prepared photocatalysts.....	34
Figure 20. Dye degradation efficiency (a) and kinetic plots (b) of the as-prepared WS ₂ /Fe ₂ O ₃ heterostructures grown at different heights.....	35
Figure 21. Schematic illustration of the proposed mechanism of MB dye photodegradation via the heterojunction WS ₂ /Fe ₂ O ₃	37

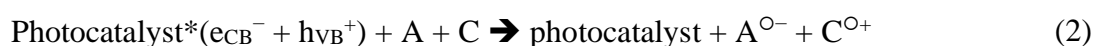
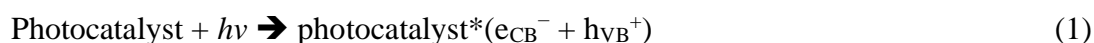
CHAPTER 1: INTRODUCTION

Nowadays, the shortage of drinkable water supply has become one of the greatest concerns globally due to the continuous massive industrial development. Supplying access to valid and clean drinking water is a must-achieved goal for the long-term economic circumstances. There are serious environmental and human health threats that contribute to water pollution such as chemical discharges including synthetic dyes, pharmaceuticals, and pesticides, in addition to heavy metal depositions and pathogenic microorganisms. Consequently, the scientific society focuses on studying and investigating powerful technologies for water purification (1–3). Synthetic dyes are widely used in coloring and printing industries, and they are usually degradation-resistant but known to be carcinogenic, which affects human's health negatively (4). Advanced oxidation processes (AOP) are employed in different technologies for water treatment including ozonation, photo-Fenton, and photocatalysis (5,6). Among these technologies, photocatalysis, especially heterogeneous photocatalysis, is considered promising as it is economic, environmentally friendly, and effective for degrading different water contaminants (7,8). The recent advancement in photocatalytic systems has brought a new era in environmental remediation as they provide highly promising potential for contaminants degradation (9).

1.1. Principle of Photocatalysis in Semiconductors

Photocatalysis is a process in which a catalyst takes in photons to initiate chemical reactions. The mechanism of photocatalysis starts with a photocatalyst absorbing a photon having an energy greater or equal to the bandgap energy of the exposed semiconductor, which excites the electrons (e_{CB}^-) at the conduction band (CB) and generates holes (h_{VB}^+) at the valence band (VB) (eq.1). Consequently, redox reactions will be initiated by these electrons and positive holes, respectively (eq. 2) where A and C are molecules present on the material's surface (10–12). After that, the

generated redox species are capable of degrading persistent pollutants in water (13).



Recently, semiconductors-based photocatalytic process has been known as a convenient approach to overcome environmental contamination problems resulting from discharging organic pollutants (14). This technology mainly involves 5 stages as shown in figure 1: i) photon absorption by the semiconducting material, ii) production of electron-hole pairs, iii) migration and recombination of the generated charge carriers, iv) reactants will be adsorbed and products will be desorbed, and v) redox reactions are conducted on the semiconductor's surface (15–17). Transition metal oxides (TMOs) show a promising potential for water treatment applications as they are chemically stable and show high photocatalytic activity (18).

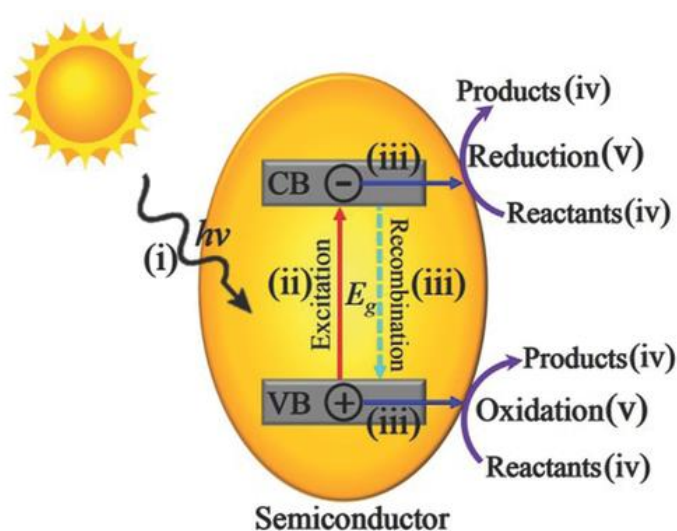


Figure 1. Schematic clarification of the photocatalytic process on a semiconductor (19).

1.2. Photocatalytic Dyes Degradation

Organic dyes contained wastewater is a consequence of major industries like textiles, food, cosmetics, and plastics (19). Usually, synthetic dyes are the main

contaminants discharged from industries and they do not biodegrade as they have increased molecular weight and degree of aromaticity, complex structure, and long-lasting stability (20,21). These dyes disturb the metabolism of the aquatic creatures by altering the biochemistry of aquatic life (22). Moreover, synthetic dyes have led to dangerous disorders and respiratory diseases in human bodies such as lung cancer and skin irritation (23,24). Low-cost techniques are required to degrade these hazardous wastes from water (25). Various techniques were developed to treat the hazardous organic dyes including adsorption, chemicals coagulation, membrane filtration, and photocatalysis. It was proved that photocatalysis is one of the most effective operations as it is simple, non-destructive, and highly efficient. Photocatalytic degradation is considered a promising degradation method that reduces the risk correlated with the existence of organic dyes in environment (26–28). Typically, dye photodegradation takes place under sunlight irradiation (29–31). It was proved that photocatalysis can fully mineralize organic contaminants and produce harmless products utilizing atmospheric oxygen alone (32,33). This powerful technology depends on the reaction conducted between organic substances and strong oxidizing and reducing agents (photogenerated e^- and h^+) (34).

Methylene Blue (MB) is classified under cationic dyes that is commonly implemented in numerous industries and a plenty of fields including chemistry and medical science. It was medically reported that the exposure to MB dye can lead several health complications in humans including nausea, corneal injury, tachycardia, and mental problems (35).

1.3. Fe₂O₃ as a Photocatalyst

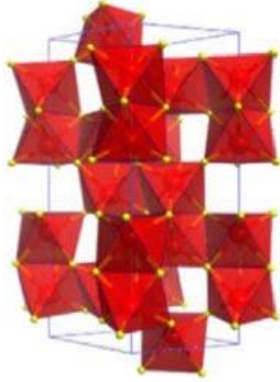
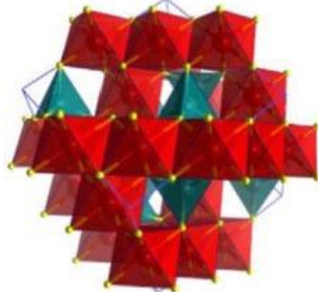
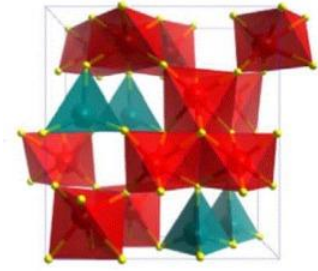
1.3.1. Structure

Iron oxides are very abundant naturally and also could be readily prepared in the laboratories (36). Fe₂O₃ is known as an n-type semiconductor and its conduction band is composed of unoccupied Fe³⁺ d orbitals, whereas the valence band consists of

full 2 t_{2g} orbitals (37). The recent research classifies Fe_2O_3 photocatalysts into different types in terms of crystal forms including: i) hematite (α - Fe_2O_3), ii) maghemite (γ - Fe_2O_3), and iii) ϵ - Fe_2O_3 (38–40). Table 1 illustrates the mentioned iron oxides and their crystal structures (38). Accordingly, each form shows distinguished properties, and the most commonly investigated are α - Fe_2O_3 and γ - Fe_2O_3 as other forms cannot be prepared as single phase materials easily (41,42).

Firstly, α - Fe_2O_3 , with its rhombohedral-hexagonal structure, is non-toxic, cost-effective, highly stable, and has a proper bandgap to be used in heterogeneous catalysis, solar cells' photoelectric electrodes, gas sensors, etc. (43,44). Also, α - Fe_2O_3 shows a corundum structure oxide having rhombohedral unit cell dimensions as $a = 5.43 \text{ \AA}$, $\alpha = 55.28^\circ$ and the lattice has space group $R3c$ (45). Hematite is the easiest form of Fe_2O_3 to synthesize because it is the final product of the thermal decay of various iron (II)- and iron (III)-containing complexes (46). Maghemite is the second most abundant Fe_2O_3 polymorph naturally in both bulk and nanosized structures. It shows a counter spinel-type structure, in which the ions are put in a ccp arrangement with $a = 8.351 \text{ \AA}$, and iron ions can be found in both octahedral and tetrahedral sites. Nanosized γ - Fe_2O_3 has magnetic and surface characteristics which makes it a useful specie for nanotechnological fields (42,47). Third, ϵ - Fe_2O_3 is a rarely formed Fe_2O_3 polymorph in nature. It shows an orthorhombic crystal structure with a value of a equals to 5.095 \AA (48). The magnetic activity of ϵ - Fe_2O_3 is not completely understood. It exhibits millimetre-wave ferromagnetic resonance and magnetoelectric which makes it beneficial in an extensive spectrum of applications like in tunable devices where electric and magnetic fields are used. However, limitations of ϵ - Fe_2O_3 could be the difficulty to synthesize a fully pure nanomaterial of it, with the least traces of other iron oxide forms. Also, synthesis challenges include low yield and thermal instability, that it instantly converts to hematite upon heating (49).

Table 1. Crystal structures of three types of Fe_2O_3 ($\alpha\text{-Fe}_2\text{O}_3$, $\gamma\text{-Fe}_2\text{O}_3$, and $\varepsilon\text{-Fe}_2\text{O}_3$) (39).

Fe_2O_3 type	Crystal structure
$\alpha\text{-Fe}_2\text{O}_3$	
$\gamma\text{-Fe}_2\text{O}_3$	
$\varepsilon\text{-Fe}_2\text{O}_3$	

1.3.2. Properties

Hematite ($\alpha\text{-Fe}_2\text{O}_3$) have drawn research efforts in the past few decades because of its exceptional ability in obtaining up to 40% of the solar spectrum, outstanding photocatalytic stability at a wide range of pH, excellent light harvesting properties as it shows convenient energy bandgap (1.9 - 2.2 eV), which makes it a promising photocatalyst for various applications. Also, it is highly abundant in nature, stable, non-toxic, and economically and environmentally friendly. However, $\alpha\text{-Fe}_2\text{O}_3$ exhibits

several limitations including high rates of charge recombination, low electrical conductivity, small hole diffusion length, and poor charge transfer kinetics (50–52). Up to now, α -Fe₂O₃ different nanostructures have been synthesized by various techniques including chemical precipitation, sol-gel processing, forced hydrolysis, hydrothermal synthesis, and microemulsion. Particularly, hydrothermal synthesis was found to be highly effective in controlling the size and shape of the synthesized nanostructure at relatively feasible conditions of time and temperature, in addition to producing highly homogenous and well-crystallized products (53–56). Hematite nanorods have been established as the most suitable nanostructure of hematite as they show relatively high surface area and increased tunability of electronic states (57). Several factors affect the photocatalytic activity of a photocatalyst including specific surface area, crystalline form, porous structure, and morphology (58,59). Previous research work reported that changing morphology may lead to changing specific area and dispersion density. As a result, photocatalytic properties are created such as charge carriers migration (60,61). Until now, a wide range of morphologies of Fe₂O₃ were obtained and studied like cubic, nanorods, nanowires, nanotubes, etc. (62). Lately, constructing heterojunctions consisting of α -Fe₂O₃ with other semiconductors is known to be an effective strategy to intensify sunlight utilization by boosting the separation of the photoproduced charge carriers, which improves the photocatalytic properties of hematite significantly (63). However, constructing photocatalysts with increased photocatalytic efficiency and recyclability is of serious challenge (64).

1.3.3. Synthesis

Various techniques have been used to synthesize nanocrystalline Fe₂O₃ including spray pyrolysis, hydrothermal methods (65), thermal decomposition (66), solvothermal (67), precipitation, and chemical vapor deposition (CVD) (68), etc. Particularly, hydrothermal synthesis was found to be highly effective in controlling the

size and shape of the synthesized nanostructure at relatively feasible conditions of time and temperature, in addition to producing highly homogenous and well-crystallized products (53–56). Hematite nanorods have been established as the most suitable nanostructure of hematite as they show relatively high surface area and increased tunability of electronic states (57).

1.4. WS₂ as a Photocatalyst

1.4.1. Structure

Transition metal dichalcogenides (TMDs) show a sort of sandwich configuration where the hexagonal layers of transition metal atoms (M) are inserted between a chalcogen placed in two layers as a sandwich configuration and produce the stoichiometry MX₂ (69). Mainly, MoS₂ and WS₂ can exist in two special phases, which are octahedral 1T phase and prismatic trigonal 2H phase (figure 2), and every phase shows distinguished properties. where 2H-WS₂ acts as a semiconductor, and 1T-WS₂ shows metallic properties. It is worth mentioning that these two phases can be converted into one another under specific conditions. For instance, 2H-MoS₂ is a semiconductor whereas 1T-MoS₂ is a conductor (70–72). The bulk hexagonal WS₂ (2H-WS₂) possesses an indirect band gap, but when it is a monolayer, it shows an indirect-to-direct transition in band gap. The lattice parameters for 2H-WS₂ are $a = 3.155 \text{ \AA}$ and $c = 12.349 \text{ \AA}$. The value of internal coordinate z of bulk 2H-WS₂ is 1.573 \AA which governs the interlayer sulfur plane distance (73,74).

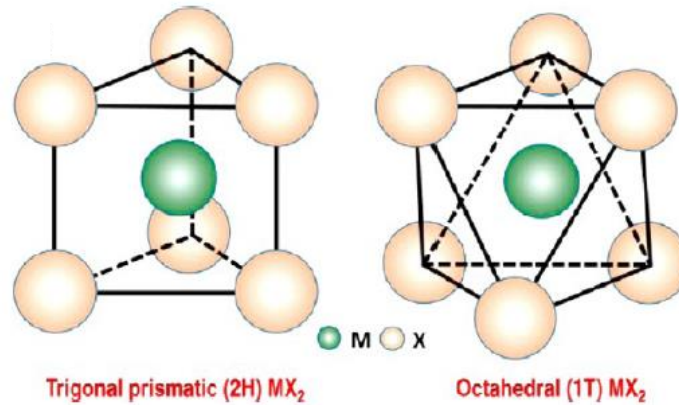


Figure 2. 2H-MX₂ and 1T-MX₂ unit cell structures (70).

1.4.2. Properties

Among two-dimensional materials, transition metal dichalcogenides (TMDs) are being studied widely because they absorb up to 10% of the visible range. Specifically speaking, MoS₂ and WS₂ show excellent photocatalytic activities, as well as an increased thermal and chemical stability. This could be accredited to the existence of many active sites such as covalent sites (S) and active metal sites (Mo or W) (75,76). TMDs can play crucial roles in photocatalytic environmental remediation, especially when coupling with another semiconducting material as they preserve activity and stability of the produced photocatalyst by offering more active sites and reducing mobility of the other component (77,78). Tungsten disulfide (WS₂) is a TMD material that has an indirect-to-direct bandgap, and is considered one of the newest generation of photocatalysts (79). It contains three S-W-S atomic planes bonded via Van der Waals forces, which makes it proper for efficient conductivity by interior to surface in electron transmission (80). WS₂ performs a transition from 1.4 eV (indirect) to 2.1 eV (direct) bandgap when the size changes from bulk into few layers causing a decrease in conduction band (CBM vs. NHE=-3.84 to -3.93 eV) and increased valence band (VBM vs. NHE=-5.82 to -5.48eV) (81–84). It shows a relatively high in-plane carrier mobility with modest Gibbs' free energy and good light matter interaction among the earth-

abundant metal composites photocatalysts (85,86). Among two-dimensional materials, WS₂ is among the most abundant naturally in Earth crust, and it is less toxic and cheaper than other TMDs. Furthermore, it is known for its remarkable properties such as high carrier mobility, increased surface area, tunable bandgap, outstanding photocatalytic and electronic properties, and biocompatibility. Also, it possesses broad absorption spectrum that makes it a light-absorbing material and hence an efficient photocatalyst. In spite of that, WS₂ has several limitations for a plenty of photocatalytic applications such as photocatalytic water splitting. This is because the band edge potential value of its conduction band minimum does not meet the requirement of that application (87). WS₂ possesses a relatively small indirect band gap that is smaller than 1.5 eV, and a high value of direct band gap that is bigger than 2 eV based on the preparation technique used (88,89). As a result, this relatively small band gap boosts up the light absorption range to 910 nm and hence allows the material to conduct redox reactions to degrade organic contaminants (90).

1.4.3. Synthesis

Several techniques have been used to synthesize WS₂, and common examples are mechanical activation technology, liquid-phase exfoliation method, hydrothermal technique, chemical deposition routes, sol-gel method, and thermal evaporation. Moreover, WS₂ can be prepared with various morphologies such as nanosheets, nanofibers, and nanorods (91).

CHAPTER 2: LITERATURE REVIEW

Extensive research works have been concentrates on how to overcome the limitations and enhance the photocatalytic properties of Fe_2O_3 and WS_2 , and among the most effective methods is constructing heterostructures (63). Taking a thorough look into the literature, limited research has been conducted in constructing Fe_2O_3 with TMDs, in general, and WS_2 , in specific, to produce an efficient photocatalyst for environmental remediation applications.

Masoumi, Tayebi and Lee succeeded in constructing a heterojunction of hematite photoanode and molybdenum sulfide (MoS_2) nanosheets. They started by growing a thin film of $\alpha\text{-Fe}_2\text{O}_3$ on FTO substrates via a simple hydrothermal process, followed by synthesizing 2D MoS_2 nanosheets through an ultrasonication-assisted liquid-phase exfoliation method. It was found that MoS_2 , a TMD material, helped in improving the photoelectrochemical performance of $\alpha\text{-Fe}_2\text{O}_3$ by lowering the rate of charge of recombination and enhancing the charge carriers separation (92). Likewise, Lejbini and Sangpour prepared MoS_2 nanosheets with $\alpha\text{-Fe}_2\text{O}_3$ nanoparticles by a hydrothermal process. The photocatalytic properties of this nanocomposite was tested towards Rhodamine Blue dye, and it showed an excellent performance compared to bare $\alpha\text{-Fe}_2\text{O}_3$ nanoparticle and MoS_2 nanosheets (93). Also, Zhang and his team synthesized a 3D flower-like structured $\text{Fe}_2\text{O}_3/\text{MoS}_2$ nanocomposite using a one-step hydrothermal rout. The researchers tested the photocatalytic properties of the produced photocatalyst against Cr(VI) under visible light irradiation (94). Similar morphology was obtained later by Alrobei, Kumar and Ram but using sol-gel method to produce $\text{MoS}_2/\alpha\text{-Fe}_2\text{O}_3$ nanocomposite. It showed a good photoelectrochemical activity for water splitting application (95).

In another study, Jia-nan, Shu, and Yong-xin used a two-step hydrothermal method to prepare $\text{Fe}_2\text{O}_3/\text{WS}_2$ heterostructure, which showed a drastically enhanced photocatalytic activity in comparison with the bare constituents. They combined Fe_2O_3

nanoparticles with WS₂ nanosheets to form a 3D flower-like morphology which caused an enhancement in separating the photogenerated charge carriers. Therefore, the obtained photocatalyst performed an efficient degradation of Methylene Blue solution, which is 5 times better than pure Fe₂O₃ and 3 times of WS₂ nanosheets alone. In addition, it showed a superior photocatalytic reduction performance on Cr (VI), which is also much better than bare Fe₂O₃ and WS₂. Figure 3 represents the proposed mechanism of the photocatalytic processes accomplished by this heterostructure (96), which is similar to the principle utilized in our study.

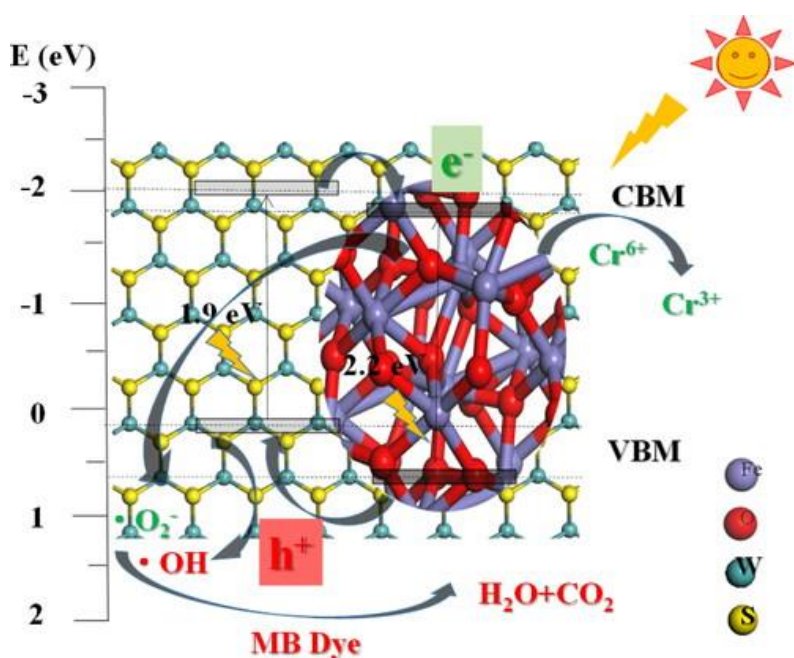


Figure 3. Schematic of the proposed photocatalytic mechanism of the photocatalyst Fe₂O₃/WS₂ (97).

Similarly, Behera and his team reported the synthesis of a heterojunction composed of vertically aligned nanorods of Fe₂O₃ by chemical bath deposition on FTO substrates, and WS₂ nanosheets prepared by hydrothermal technique. This produced heterojunction exhibited an improved photoelectrochemical activity for water splitting (97). Another study reported core-shell constructed α -Fe₂O₃/WS₂/WO_x nanorods by growing WS₂ nanosheets on α -Fe₂O₃ photoanodes. The WS₂ nanostructures were

synthesized via liquid-phase exfoliation method (LPE), whereas hematite NRs were prepared hydrothermally. This core-shell photoanodes showed an outstanding separation, reduced recombination rate of the photo-produced charge carriers, and improved electron transport activity. These advantages contributed effectively to the photoelectrochemical (PEC) performance. The most efficient prepared photoanode was $\alpha\text{-Fe}_2\text{O}_3/\text{WS}_2/\text{WO}_x$ achieved up to 30-fold better than that of bare $\alpha\text{-Fe}_2\text{O}_3$ (98).

Taking a general review on the photocatalytic applications of hematite in the literature, certainly for water treatment, a variety of research work was done to understand and employ hematite in this field. It can be noticed that constructing heterostructures of hematite with other nanomaterials with photocatalytic properties makes a significant improvement in the activity of the obtained photocatalyst.

For example, Sun, Jia, Wang, and others constructed a Z-scheme $\alpha\text{-Fe}_2\text{O}_3/\text{g-C}_3\text{N}_4$ composite via ultrasonic and calcination processes. The highly active hollow $\alpha\text{-Fe}_2\text{O}_3$ (S3) sample was prepared using H_2PO_4^- and Cu^{2+} ions by hydrothermal technique. It is worth mentioning that the obtained hollow S3 has a large surface area and high O_v concentration which results in an improved photocatalytic degradation activity. The researchers synthesized S3/ g- C_3N_4 composites in different mass ratios of S3 and g- C_3N_4 of 0.1:1, 0.2:1, 0.3:1, and 0.4:1, then labeled them as 0.1-1FCN, 0.2-1FCN, 0.3-1FCN, and 0.4-1FCN, respectively. The prepared heterojunctions showed an outstanding visible-light photocatalytic performance by intensifying the separation ability of the photogenerated charge carriers as well as the production of active species. The study tested the photocatalytic degradation efficiency of the composite against p-Nitrophenol which is a highly toxic organic contaminant in water and non-biodegradable (99). Another example is heterostructuring $\alpha\text{-Fe}_2\text{O}_3$ with ZnO, another TMO, which was achieved by Harijan et al. via a facile and simple route which is the thermal decomposition of Fe (II) oxalic acid complex at 500°C followed by

precipitation of ZnO nanoparticles at 90°C with different ratios (α -Fe₂O₃: ZnO = 1:1, 2:1, and 1:2). α -Fe₂O₃ – ZnO composite exhibited an outstanding photodegradation efficiency of methylene blue under UV light compared to pure α -Fe₂O₃ and ZnO, where the ratio 1:2 represented the highest efficiency among all samples. Moreover, Alhabradi et al. succeeded in fabricating CdO decorated α -Fe₂O₃ thin film nanorods arrays via throughput radio frequency (RF) sputtering. Hematite thin films were synthesized in different thicknesses of Fe ranging from 10 to 150 nm, where 70 nm exhibited the highest photocurrent density. The composite exhibited an enhanced MB dye degradation performance (98% in 40 minutes), which is higher than bare α -Fe₂O₃ which showed 60% in 40 minutes (100).

For pharmaceuticals degradation using hematite heterostructures, many work also was achieved. For instance, a study done by dela Rosa et al., amoxicillin (AMX) was degraded phototactically using TiO₂/Fe₂O₃ sandwich-type composites synthesized in different configurations. These composites were fabricated via spin coating. The photocatalytic activity of prepared heterojunctions was studied under simulated solar irradiation in the presence and absence of persulfate (PS). This research approved that TiO₂@ α -Fe₂O₃ sandwich-type composite achieved the best photodegradation performance of AMX with enhanced performance in the presence of PS. This superior performance was attributed to the excellent charge separation achieved via TiO₂@ α -Fe₂O₃ heterojunction compared to the other tested photocatalysts. SEM imaging illustrated the thickness of the prepared layers that was within (1.06±0.20 μ m). The recorded results were normalized to the degradation extent obtained by TiO₂-P25 which was considered the benchmark photocatalysts. Moreover, the biodegradability of AMX solution was enhanced significantly due to mineralization by the hydroxylation pathway, which adds precious value to this study (101).

In a similar aspect, Qiu et al. synthesized Fe₂O₃/Co₃O₄ nanosheet arrays on

nickel foams using a facile approach. The surface morphology of the prepared nanomaterial was demonstrated using SEM. The heterojunction $\text{Fe}_2\text{O}_3/\text{Co}_3\text{O}_4/\text{NF}$ showed several benefits including narrow bandgap energy and an increased separation rate of the photo-produced charge carriers. It was found that this photocatalyst photodegrades sulfamethoxazole (SMZ) with the highest catalytic efficiency compared to each component alone. This outstanding activity was attributed to the unique Z-scheme heterostructure that facilitated the visible light absorption and the transfer of photo-generated charge carriers resulting from the staggered energy band structures of Co_3O_4 and Fe_2O_3 . In addition, nickel foam worked as an excellent electron mediator and supported to improve the performance and stability of $\text{Fe}_2\text{O}_3/\text{Co}_3\text{O}_4$ nanocomposite. For future work, this study introduced a reference in constructing a Z-scheme heterojunction to produce efficient and stable semiconductor photocatalysts (64).

Looking at the research work achieved on degrading methylene blue (MB) dye from aqueous solutions, several technologies have been employed like chemical coagulation, membrane filtration, and using adsorbents. Table 2 summarizes some of the recent studies done on MB dye degradation in wastewater, including this study, in order to compare between the different technologies used in terms of efficiency.

Table 2. Different techniques for MB dye degradation from wastewater in recent studies.

Treatment technique	Material	Performances	Ref.
Photo-Fenton-like reactions	$\alpha\text{-Fe}_2\text{O}_3$ catalyst	60% discoloration efficiency at 120 min	(102)
Electrocoagulation	Anode: iron rod electrode Cathode: graphite rod electrode	Decolorization rate is 63.24% at pH=9	(103)
Ultrafiltration membrane in a photoelectrocatalytic cell	Ti/TiO ₂	Colour removal efficiency 64.19%	(104)

Photocatalysis	WS ₂ /Fe ₂ O ₃	Photodegradation efficiency 69.4% in 125 min	This study
----------------	---	---	------------

It is worth noting that ultrafiltration technique requires additional chemical agents to aggregate MB dye molecules. Also, using Fenton's reagent could generate sludge that results in sludge disposal issue and requiring a strict pH control. On the other hand, photocatalysis is rapid, cost-effective, and does not produce secondary waste (105).

CHAPTER 3: EXPERIMENTAL METHODOLOGY

3.1. Materials Synthesis Methods

3.1.1. *Hydrothermal Technique*

Hydrothermal method is among the most common routes for synthesizing nanomaterials. It is used extensively to synthesize a plenty of metal oxide nanostructures. It is known as one of the most convenient, simple, and a solution

reaction-based approach. Particle size, morphology, and chemistry of the prepared nanomaterials can be adjusted by modifying different reaction parameters including the concentration of precursors, growth time, and reaction temperature. This type of techniques can take place in wide range of temperatures ranging from room temperature to very high temperature (106,107). This method involves placing precursors such as metal salts in water inside a closed reaction autoclave and then exposing it to high temperature and pressure (108). Typically, an outer jacket and a Teflon tube is used as a container for the reactors (109). The set up of a hydrothermal experiment is shown in figure 4.



Figure 4. The setup used for hydrothermal method.

3.1.2. Chemical Vapor Deposition (CVD)

Among the most useful techniques for preparing high-quality large scale mono- and few-layered TMDs is chemical vapor deposition (CVD) technique, which is classified as a “bottom-up” method (110). In this technique, TMD precursors react and deposit on the exposed substrate at high temperature as mono- or few-layer film. Previous research works obtained TMDs nanostructures that achieved outstanding photocatalytic properties with tunable thickness, high crystal quality, and scalable size (111,112). CVD can be used to grow a TMD material via various routes. The route followed in this

work involved vapor phase reaction of two precursors: the chalcogen and the transition metal oxide precursors under a certain gas flow (113). The morphologies of the constructed TMDs layers depend on several growth conditions such as the substrate's nature, gas flow rate, precursors ratio and concentrations, and temperature. In addition, the distance between the TMD source and substrate was found to play a significant role in morphology control (114–116). Figure 5 shows the CVD system used which consists of a Lindberg Blue M tubular furnace, quartz tube with a diameter of 2-inch, gas cylinders, pumping system that are all controlled by Flow Vision software.

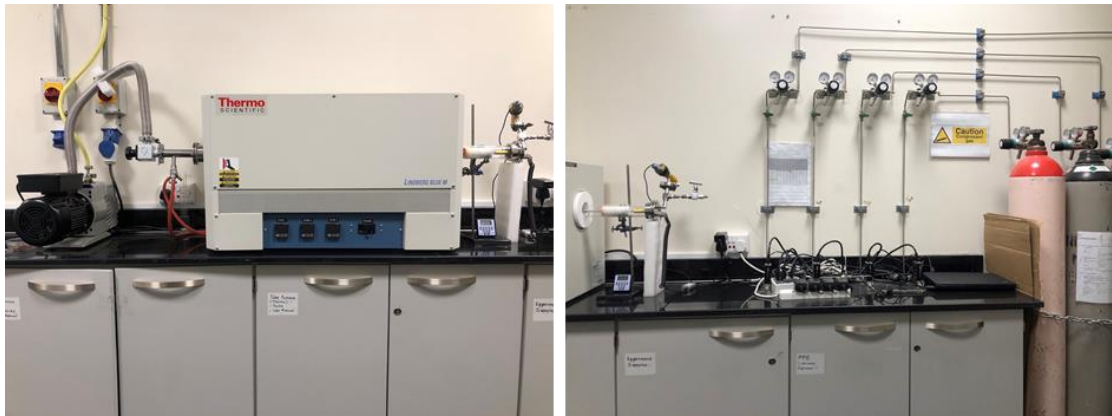


Figure 5. The used CVD system.

3.2. Materials Characterization Techniques

Several methods were implemented to characterize and investigate the properties of the prepared nanomaterials including morphology and structure.

3.2.1. X-Ray Diffraction

X-Ray Diffraction (XRD) is characterization method that provides information on the structural parameters such as crystal defects, grain size and crystallinity without destructing the sample. Also, it gives information about the preferred crystal orientations. XRD applies incident X-ray on the material and then measures the intensities and the angles of the leaving scattering X-ray (117). The angle lies between the incoming and leaving X-ray irradiation is called 2θ , and the distance between the

sheets of charge is d as shown in figure 6 (118). Therefore, Bragg's Law can be applied when a constructive interference is observed:

$$n \lambda = 2 d \sin \theta \quad (1)$$

Where n is an integer (1, 2, 3,...), λ is the X-ray beam's wavelength, and θ is the half of the scattering angle as illustrated in figure 6 (119).

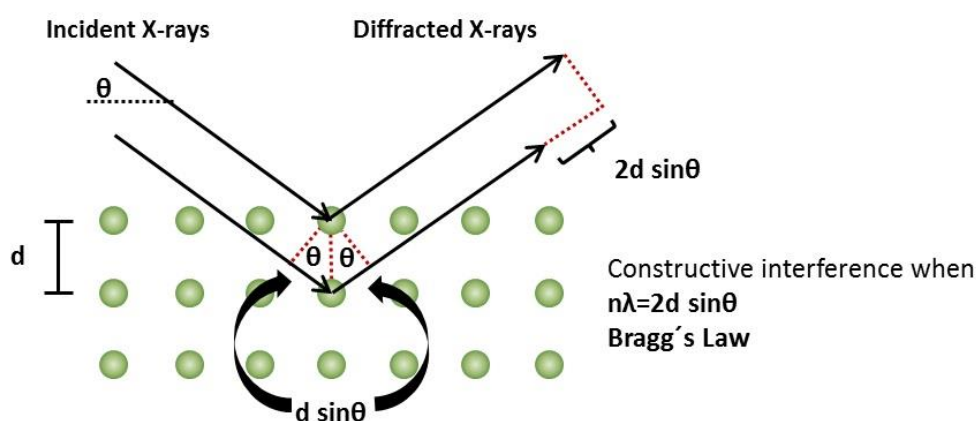


Figure 6. Schematic explanation of Bragg's Law (114).

Instrument

The used XRD instrument was PANalytical by EMPYREAN X-Ray diffraction, 40 KV/30 mA, uses the Cu-K α radiation ($\lambda = 1.54056 \text{ \AA}$) having the scan rate of $2^\circ/\text{min}$.

3.2.2. Raman Spectroscopy

Raman spectroscopy is a major spectral analysis technology for investigating chemical bonds, chemical composition, and structural information of material (120). Raman effect takes place when the specimen is irradiated by an intense monochromatic irradiation. Photon-molecule interactions cause what is called Raman scattering, which is a two-photon process (121). In this case, the photon could excite a molecule from the ground state to a virtual energy state. Then a photon will be released from the relaxed molecule, and it goes back to a different vibrational or rotational state. Eventually, if the energy state is higher than the starting state, the released photon of a

less frequency creates a Stokes line. However, if the molecule loses energy, the emitted photon of a lower frequency creates an anti-Stokes line. Figure 7 spotlights the possible scattering styles in Raman spectroscopy. Generally, Raman (wavenumber) shifts reflect analytical characteristics on variations between the quantum levels of each substance and hence play a crucial role in substance identification. Generally, Raman spectrum correlates the intensity of the scattered light (in arbitrary units) with wavelength or Raman frequency shift in cm^{-1} (122).

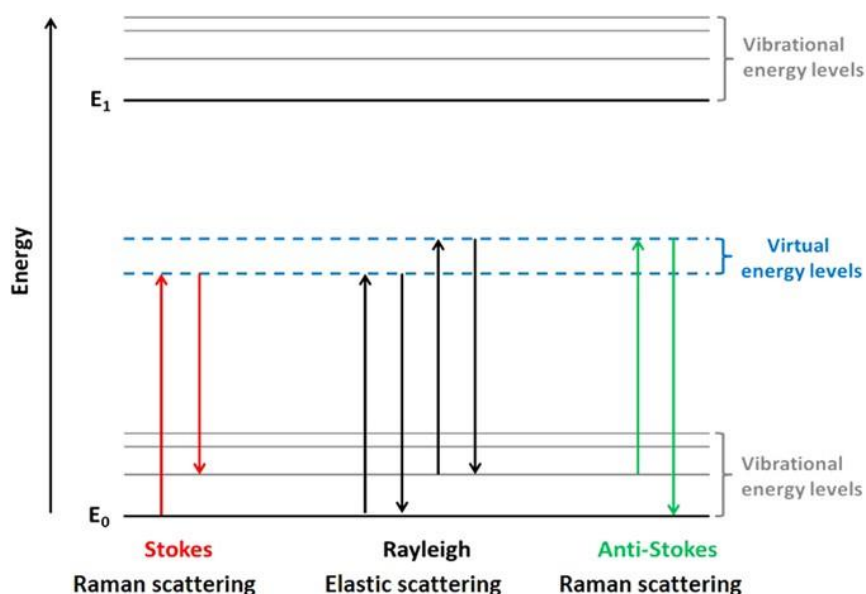


Figure 7. Schematic illustration of the scattering types in the Raman spectroscopy (118).

Instrument

Thermo fisher scientific DXR Raman Microscope having the wavelength of 532nm, 40 times scanning, with a laser power of 10, 50x.

3.2.3. Scanning Electron Microscopy (SEM)

SEM technique can yield information on the specimen's surface topography, crystalline structure, chemical identity, and electrical properties of about 1 μm of the specimen's upper part. This technique can achieve up to 1,000,000x magnification. Typically, an electron gun is used to generate electron beam with energies 2-40 keV towards the

sample, and several interactions will be produced that includes secondary electrons, backscattered electrons, Auger electrons, and x-ray irradiation as seen in figure 8. The different types of obtained electrons can be detected using various detectors to produce images and give a certain piece of information about the specimen. Firstly, secondary electrons (SE) are those that leaves the specimen with energies lower than 50 eV, mainly left their orbits because of the incident electron. This type of electrons produces topographic information. Backscattered electrons (BSE) are the same incident electrons that were able to approach the nucleus of an atom and then be scattered and re-emerge from the specimen's surface with much higher energy than SE. Mainly, BSE provide information on the chemical composition depending on the atomic mass of the element. Also, they can provide crystallographic information of the desired material (123).

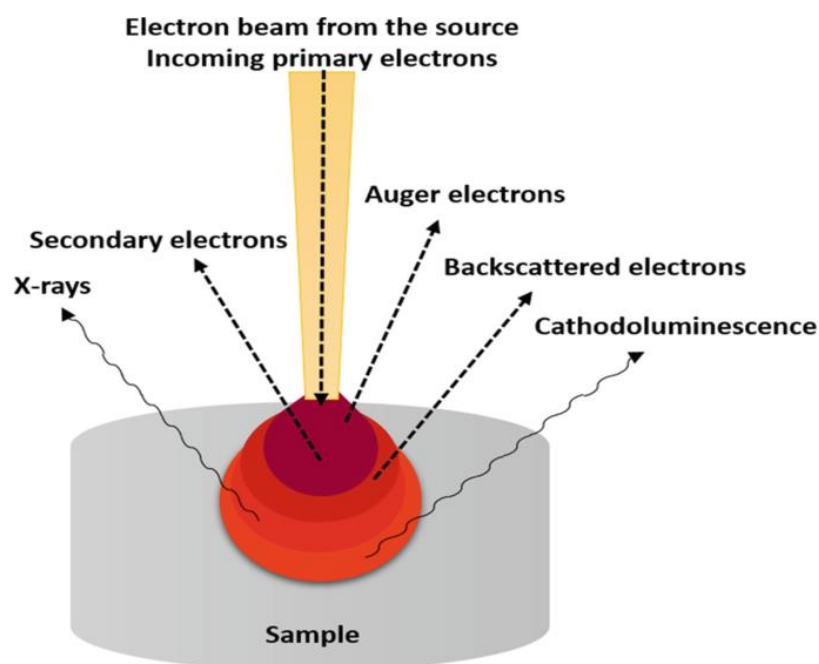


Figure 8. Schematic of various primary electron beam interactions with the specimen (120).

Instrument

SEM instrument by FEI NOVA NANOSEM 450, working at 0.5-30 kV of acceleration voltage.

3.2.4. X-ray Photoelectron Spectroscopy (XPS)

X-ray photoelectron spectroscopy (XPS) is a highly useful technology that produces information on the surface composition of the specimen. The elemental and chemical composition of the sample can be detected by using X-ray radiation to provide enough energy to accommodate the binding energy (BE) of the core electrons and excite them. Sensitive detector will calculate the kinetic energy of the produced electrons, which is a characteristic property for each element. The binding energies can be determined from the peak position, and the elemental composition and oxidation states possessed by the sample can be identified (124).

CHAPTER 4: RESULTS AND DISCUSSION

4.1 Synthesis of Fe₂O₃

4.1.1. Materials

Iron (III) chloride hexahydrate FeCl₃.6H₂O (VWR International bvba Geldenaaksebaan), Sodium nitrate NaNO₃ (VWR International bvba Geldenaaksebaan) and Hydrochloric acid HCl (37%, Analar NORMAPUR), were used as sources for the hydrothermal synthesis. Before the growing the desired material, acetone, ethanol, and deionized water were used to clean FTO substrates which were put in ultrasonic bath for 15 min each. After that, nitrogen gas was used to dry the substrates.

4.1.2. Fe₂O₃ NRs synthesis method

The synthesis of Fe₂O₃ NRs was achieved by hydrothermal technique as suggested by Masoumi et al, (92,98). First, a 30 ml aqueous solution of the mixture Iron (III) chloride hexahydrate and sodium nitrate in the ratio 0.15:1 respectively was freshly prepared. Then 2 drops of HCl were added to the homogenous solution so the pH value of the mixture is equal to 1.5. After that, the clean FTO substrates were placed in a 100 mL Teflon-lined stainless-steel autoclave, with placing the conductive side of FTO

substrate facing the walls of the Teflon beaker, and the produced solution was then poured into it. The hydrothermal preparation took place inside an oven at 100⁰C for 6 hrs. At this stage, FeOOH is formed. To grow Fe₂O₃ NRs, the as-prepared samples were annealed under air inside a furnace at 550⁰C for 4 hrs. The effect of two factors on the NRs' morphology was investigated which are precursors' ratio and annealing temperature. Precursors' ratio (NaNO₃: FeCl₃) varied as following: 0.15:1, 0.15:0.6, 0.15:0.8, 0.15:1.2, and 0.15:1.4. Furthermore, annealing temperature was also investigated as follows: 500, 600, 650⁰C in addition to the original temperature 550⁰C.

The synthesis of Fe₂O₃ on FTO substrates was confirmed by several characterization techniques including SEM images (figure 9) that show the presence of the nanorods with an average length of 0.375 μm. The nanorods surfaces are covered with pores which are believed to be resulting from the dehydration during the thermal treatment as stated by the following chemical equation:

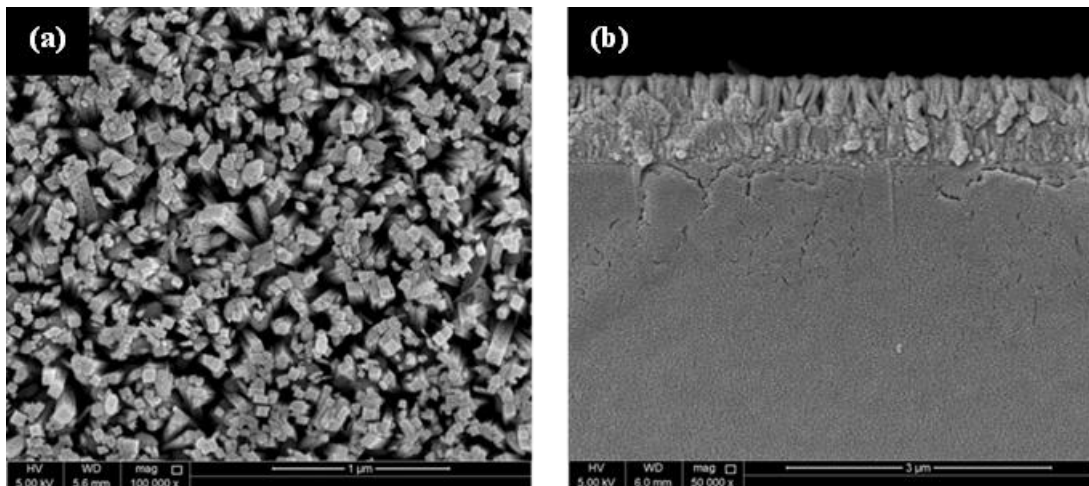
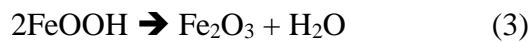


Figure 9. SEM images of top view (a) and cross section (b) of as-prepared α -Fe₂O₃ NRs.

Moreover, the Raman and XRD were employed to confirm the presence of Fe₂O₃. Raman spectrum in figure 10a exhibits several peaks for Fe₂O₃ at 223 (A_{1g}), 247

(E_g), 290 (E_g), 408 (E_g), 609 (E_g), and 658 (LO E_u) cm⁻¹ (125). On the other hand, XRD pattern in figure 10b shows four diffraction peaks at 33.8°, 35.4°, 42.8°, 54.7°, 61.7°, 64.0°, and 78.4° corresponding to hematite crystal planes of (104), (110), (113), (116), (214), (300), and (1010) respectively (JCPDS file no.33-0664) (126).

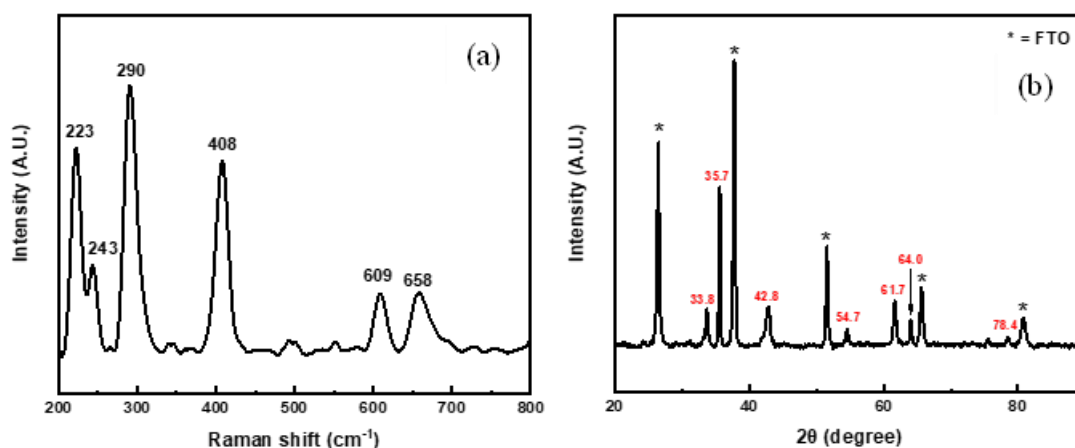


Figure 10. Raman spectrum (a) and XRD pattern (b) of Fe₂O₃ NRs.

4.1.2.1. Precursors' Ratio Effect

The precursors ratio (NaNO₃: FeCl₃) was investigated as an influencing factor on the synthesis of Fe₂O₃ NRs. It was confirmed that this factor affects the morphology of the NRs as SEM images suggested in figure 11. The amount of NaNO₃ seem to influence the morphology of the NRs. By the amount of NaNO₃ increases, the NRs get more uniform in shape, and the holes appearance decreases. This change is expected to decrease the photocatalytic activity of the NRs because it is believed that the abundance of through-holes contributes to the enhancement of photocatalytic properties of the hematite nanorods as stated by Liu et al (127).

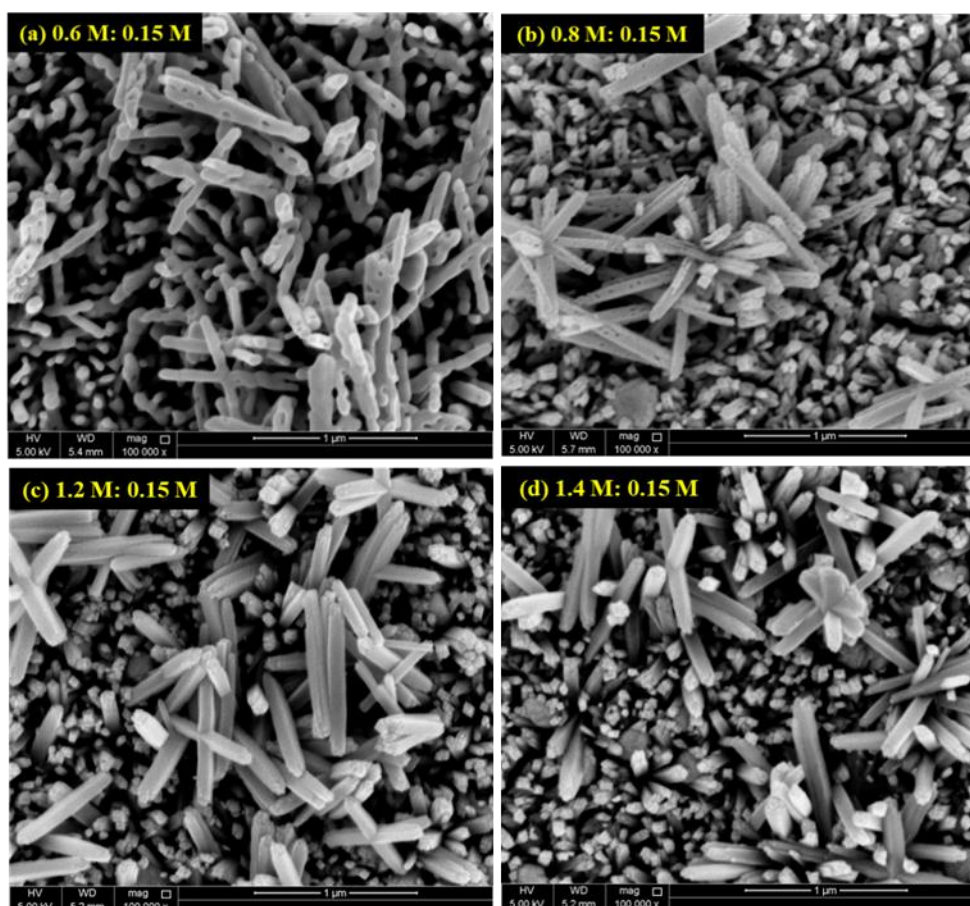


Figure 11. Surface SEM images of different precursors ratios of NaNO_3 : FeCl_3 .

4.1.2.2. Annealing Temperature

Annealing is a crucial process in hematite synthesis as it undergoes the transformation from FeOOH formed in the hydrothermal process into $\alpha\text{-Fe}_2\text{O}_3$ NRs. This study proves that annealing temperature contributes significantly to the NRs formation, and this can be seen in the change in morphology. The thermal treatment dehydrates the NRs and hence forms holes covering each nanorod (127). Annealing at 500°C did not provide sufficient heat to create the holes as can be observed in figure 11a. On the other hand, annealing at 600°C and 650°C started to cause a deformation of the nanorods as illustrated in figure 11 (c, d). The reference recipe in this study uses 550°C as annealing temperature that allows creating holes in NRs without resulting in deformation as represented previously by figure 9.

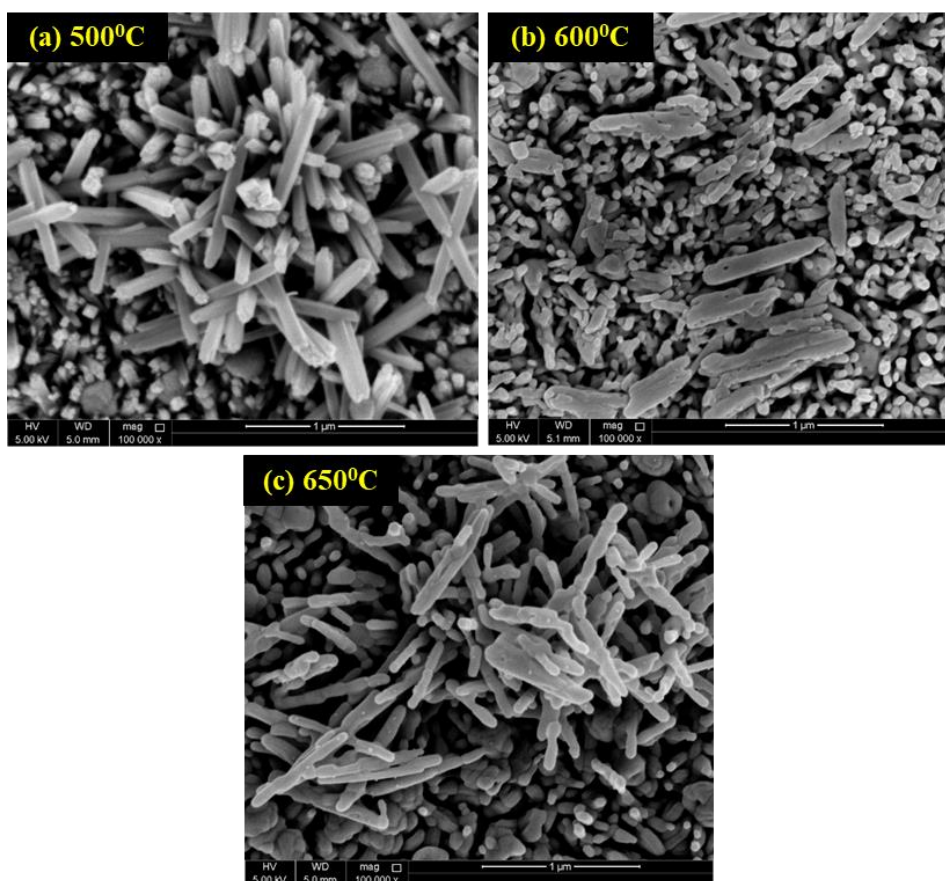


Figure 12. Surface SEM images of hematite NRs annealed at three different temperatures.

4.1.3. Photodegradation of Methylene Blue

The photocatalytic degradation performance of the prepared Fe_2O_3 NRs was tested against MB dye by tracking photo-assisted degradation. Xe arc solar simulator of 150 W was used to perform the photodegradation examination as the irradiation source, where each sample was placed in 50 ml of 10 ppm of MB dye solution with continuous stirring. Before exposing the sample to the radiation, the sample was placed in dark for 25 minutes. After that, the solution was subjected to a simulated solar radiation 11 cm above the solution surface as shown in figure 13. Every 25 min for 125 min, 3 ml of this dye solution was taken to measure its absorption spectra at the lambda max of the MB dye which is located at 664 nm. The instrument used to track the

photocatalytic performance of the samples was UV-visible spectrophotometer by JASCO: V-570, Japan.

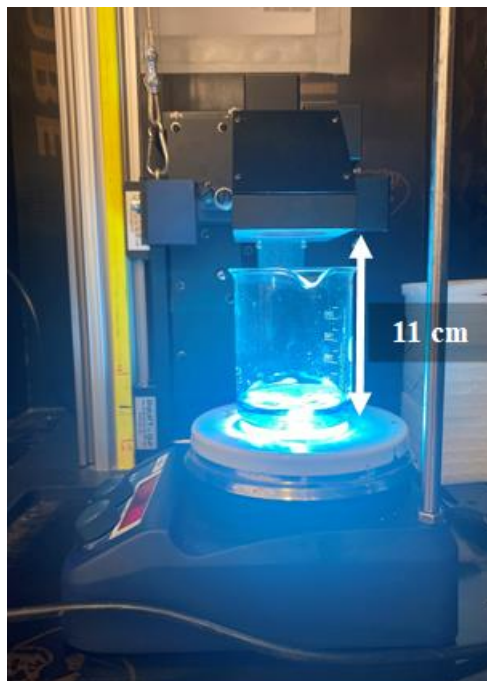


Figure 13. The used experimental setup for the photodegradation of MB by the prepared photocatalysts.

4.2. Construction of $\text{WS}_2/\text{Fe}_2\text{O}_3$ Heterostructures

Chemical vapor deposition (CVD) is among the most useful and common techniques for two-dimensional transition metal dichalcogenides (TMDCs) synthesis with different morphology, size, and crystal quality, which can be employed in a plenty of research fields and applications. However, coupling 2D tungsten disulfide (WS_2) with a TMO like Fe_2O_3 considering a controlled orientation and size is still a challenging issue. In this section, we illustrate a controllable synthesis of WS_2 flakes on Fe_2O_3 nanostructures by optimizing the CVD growth conditions.

4.2.1. Materials

The precursors used were high-purity tungsten trioxide (WO_3) powder (99.97%, Sigma Aldrich), and sulfur (S) powder (99.5%, Sigma Aldrich). The substrates utilized

were Fluorine doped tin oxide (FTO) glass. Prior to the growth, FTO substrates were cleaned using a 15-min sonication in acetone, ethanol then deionized water using ultrasonic bath. After that, drying the substrate took place using nitrogen flow. Argon gas (99.99%) and mixed gas (H_2 : Ar) were used as the carrier gases.

4.2.2. Preparation of WS_2/Fe_2O_3 Heterostructures

For the synthesis of WS_2/Fe_2O_3 heterostructures, the as-synthesized Fe_2O_3 NRs samples were used as substrates for the growth of vertical WS_2 nanoflakes via CVD on the Fe_2O_3 NRs. The growth of WS_2 nanoflakes was achieved using Lindberg Blue M CVD system that includes a quartz furnace tube with a diameter of 2 inches. For a typical growth, the FTO substrate covered with Fe_2O_3 NRs was placed with its conductive side facing downwards to a 10-cm long alumina ceramic boats that contains 70 mg of WO_3 powder. This boat of WO_3 with the mounted substrate was placed at the center of the furnace, while a ceramic crucible holding 700 mg of the powder of sulfur was placed upstream at 15-cm distance of from the WO_3 source. After 30 min of evacuating the system, the reactor was purged with 100-sccm high-pure argon gas for 15 minutes. Then the temperature of the furnace was raised up to $675^\circ C$ with a ramping rate of $15^\circ C/min$. At that temperature, the growth of WS_2 took place under the flow of 100 sccm Argon and mixed gas (60 Ar: 40 mixed gas) for 40 minutes. Meanwhile, the temperature of sulfur crucible, which was monitored by separate thermocouple, reached $180^\circ C$. When growth time was over, the reactor was cooled down under the flow of 100 sccm Argon flow. Several runs were conducted where the WO_3 powder was placed in different heights inside the boat in order to study the effect of changing the distance between the substrate and the precursors. Figure 14 illustrates the experimental setup configuration.

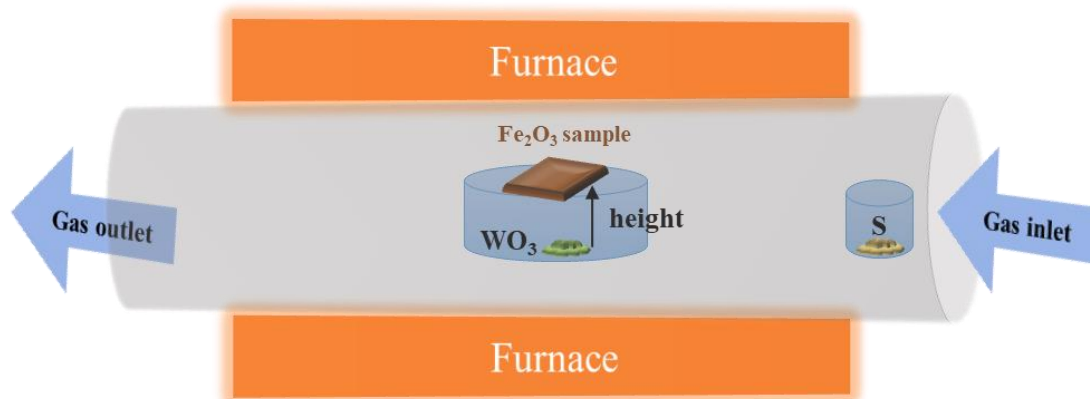


Figure 14. Schematic of the used experimental setup in CVD.

To improve the photocatalytic activity of Fe_2O_3 , a heterostructure of $\text{WS}_2/\text{Fe}_2\text{O}_3$ was constructed via CVD growth of WS_2 flakes on previously grown Fe_2O_3 NRs film. The effect of the distance between Fe_2O_3 sample and the tungsten precursor was investigated to obtain an optimized growth of WS_2 nanoflakes in the heterostructure. Figure 15 illustrates the SEM surface images of the constructed $\text{WS}_2/\text{Fe}_2\text{O}_3$ at three different vertical distances (heights). A significant effect on the growth of WS_2 nanoflakes was observed. SEM images revealed that the size and density of WS_2 nanoflakes decreases with increasing the distance between the Fe_2O_3 sample and the tungsten precursor. In figure 15a, the lowest distance showed the biggest size and the highest density of the vertically aligned WS_2 flakes that fully covered the grown Fe_2O_3 nanostructures, whereas the flakes are less dense in figure 15b when the height is higher. This allowed the observer to barely see the Fe_2O_3 nanorods underneath. However, both nanostructures can be observed and distinguished clearly in figure 15c where the height is the highest as the WS_2 flakes show the lowest size and density. In figure 15d, WS_2 nanoflakes are not clearly observed and this is an indication of an incomplete growth of the material on Fe_2O_3 , which is expected to negatively affect the photocatalytic activity of the sample. It is worth mentioning that Fe_2O_3 NRs deformation was noticed in figure 15c, which suggests that the CVD conditions could

affect the morphology of hematite during the synthesis of WS₂ and constructing the heterostructure due to additional thermal treatment in CVD reactor. To sum up, SEM images suggest that optimizing the height produces a controllable growth over the size of WS₂ nanoflakes constructed on Fe₂O₃ NRs.

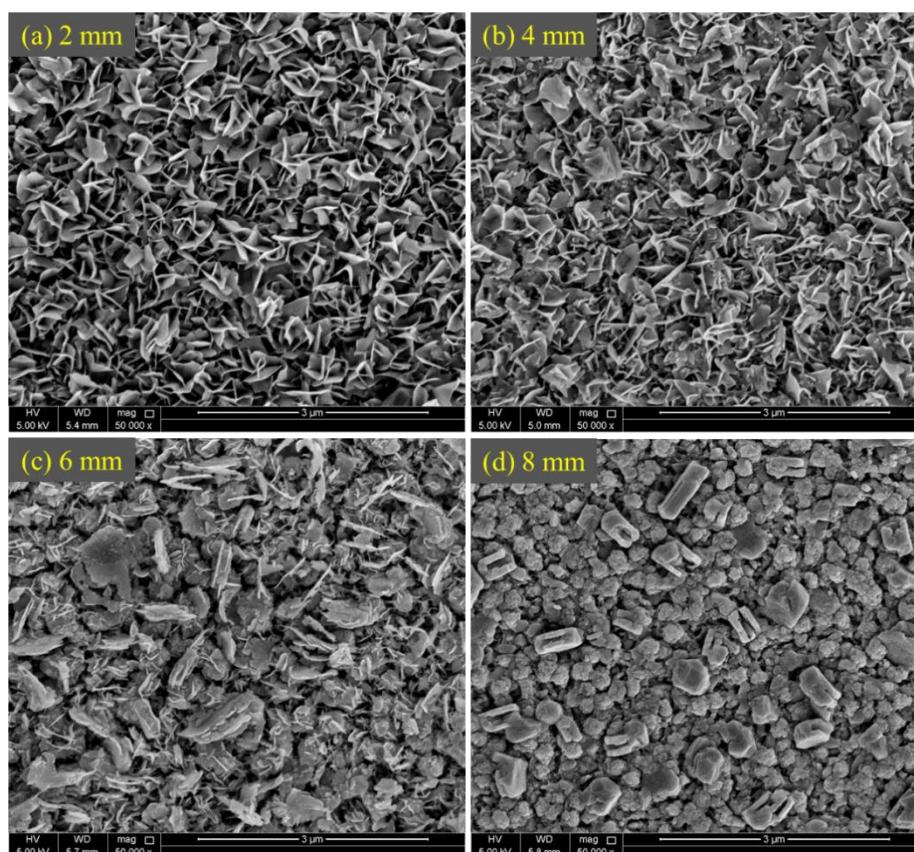


Figure 15. SEM surface images of WS₂/Fe₂O₃ heterostructures constructed at 4 different heights.

Raman spectra and XRD patterns were used to prove the formation of the heterostructure grown using 6 mm height. Figure 16a shows the Raman spectra where the three peaks can be observed at around 319, 345 and 414 cm⁻¹, that correspond to LA(M) + ZA(M), E_{2g}¹(Γ) and A_{1g}(Γ) modes for WS₂, respectively. Moreover, the spectrum exhibits two main peaks for Fe₂O₃ active modes at 227 cm⁻¹, and 291 cm⁻¹, correlating with A_{1g} and E_{1g}, respectively. XRD pattern is demonstrated in figure 16b

for the as-synthesized WS₂/Fe₂O₃ heterostructure. The diffraction peaks at 14.2°, 33.7°, 61.6°, and 80.6° can be attributed to (002), (101), (008) and (0010) planes of WS₂ (JCPDS file no. 08-0237). Also, the pattern shows four diffraction peaks at 35.4°, 42.8°, 54.6°, and 75.4° corresponding to Fe₂O₃ crystal planes of (110), (113), (214), and (1010) respectively (JCPDS file no.33-0664). Subsequently, the constructed heterostructure sample shows Raman and XRD characteristics of both WS₂ and Fe₂O₃, which is an indication of the successful growth of WS₂ nanoflakes on Fe₂O₃ nanostructures.

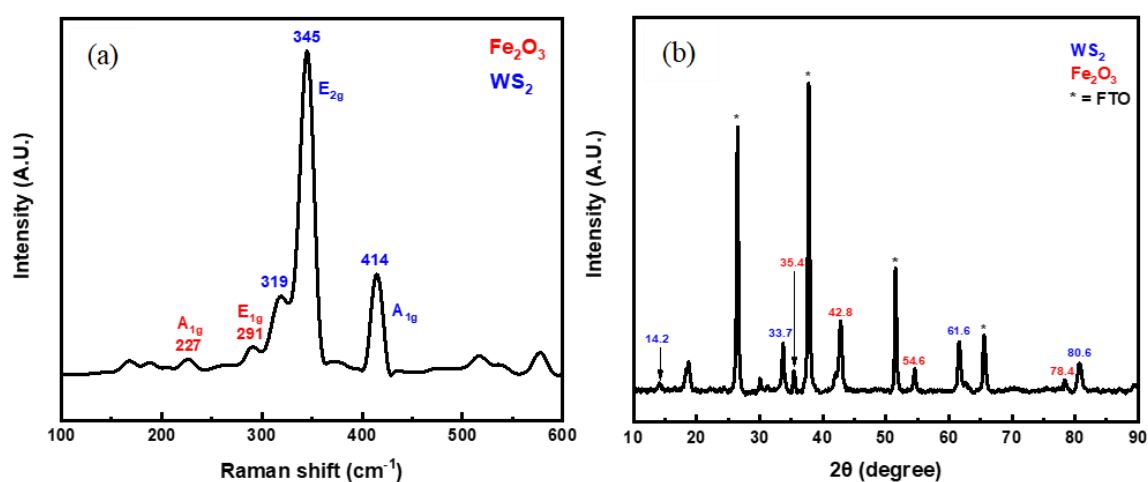


Figure 16. Raman spectrum (a) and XRD pattern (b) of WS₂/Fe₂O₃ heterostructure.

For further examination of the chemical states and the surface composition of the prepared heterostructure WS₂/Fe₂O₃, XPS technique was implemented as illustrated in the XPS spectra in figure 17. The full spectrum is shown in figure 17a. Figure 17b shows the high-resolution spectrum of W 4f where three peaks can be observed at 34.4 and 36.6 eV, which represent W 4f_{7/2} and W 4f_{5/2} corresponding to W⁴⁺ oxidation state, as well as a peak at 38.3 eV which correlates to W⁶⁺ indicating the presence of a trace amount of WO₃ that did not react (128). The high-resolution spectrum of sulfur is shown in figure 17c where two peaks are identified at 168.2 and 168.8 eV which emerged from the existence of S²⁻ valence state in the heterojunction

sample (129). In figure 17d, the binding energy values at 709.0 and 711.6 eV correspond to Fe 2p_{3/2} for Fe³⁺ and Fe²⁺ respectively, whereas the peaks at 722.6 and 732.5 eV correspond to Fe 2p_{1/2} (130). The peaks shown in figure 17e belong to O1s at 528.9 and 530.9 eV that indicate the presence of the lattice oxygen in Fe-O and as chemisorbed oxygen participating as a hydroxyl group (131).

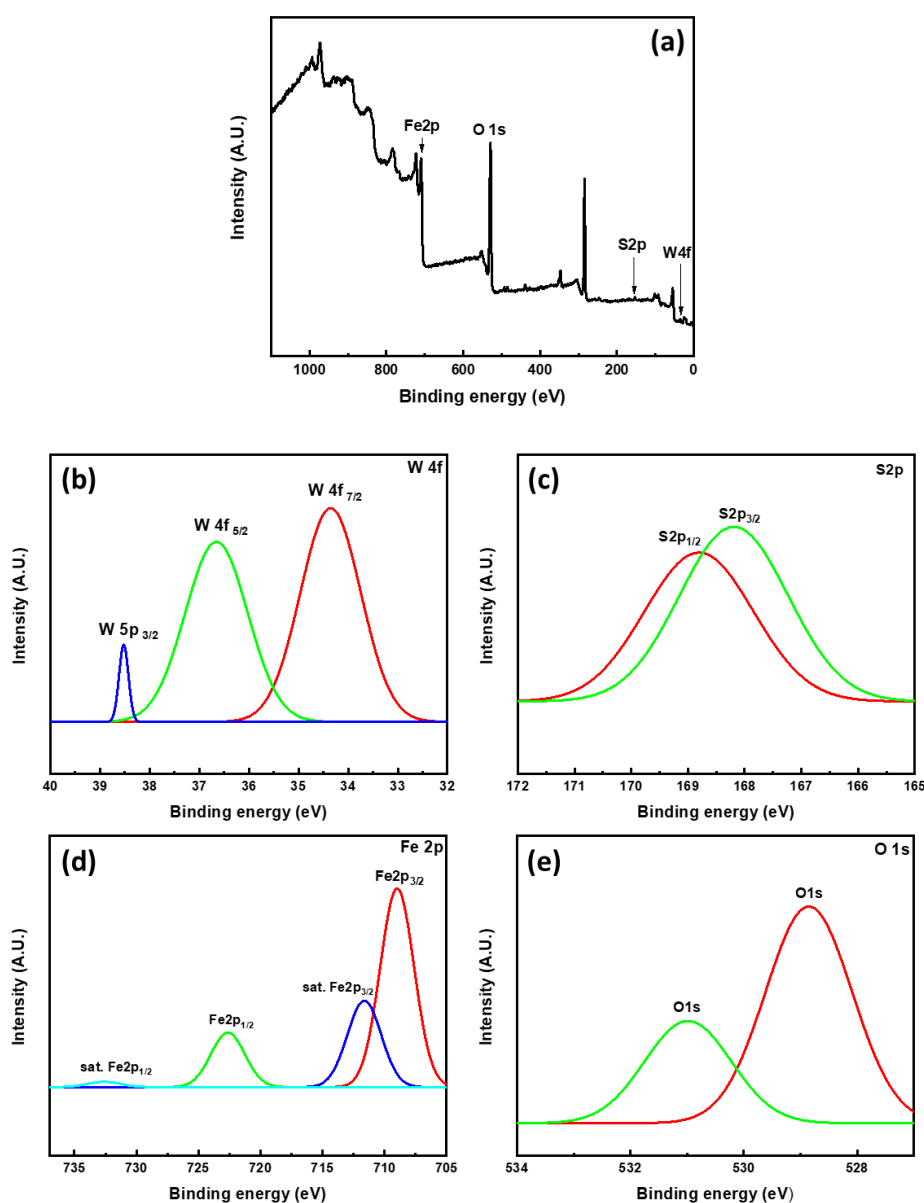


Figure 17. XPS spectra of the heterostructure $\text{WS}_2/\text{Fe}_2\text{O}_3$ (a), W 4f (b), S 2p (c), Fe 2p (d), and O 1s (e).

The photocatalytic properties of the as-synthesized heterostructures were tested against MB dye and the photodegradation activity was studied under solar simulator irradiation. For the sake of comparison, figure 18a shows the absorption spectra of the MB dye degradation using an Fe_2O_3 sample, whereas figure 18b is absorption spectra under WS_2 photocatalyst. Figure 18c shows the absorption spectra of the MB dye degradation using a 6 mm height $\text{WS}_2/\text{Fe}_2\text{O}_3$ sample as a photocatalyst. It can be seen

clearly that a significant enhancement was achieved by coupling Fe_2O_3 with WS_2 in an active heterostructure over each component alone.

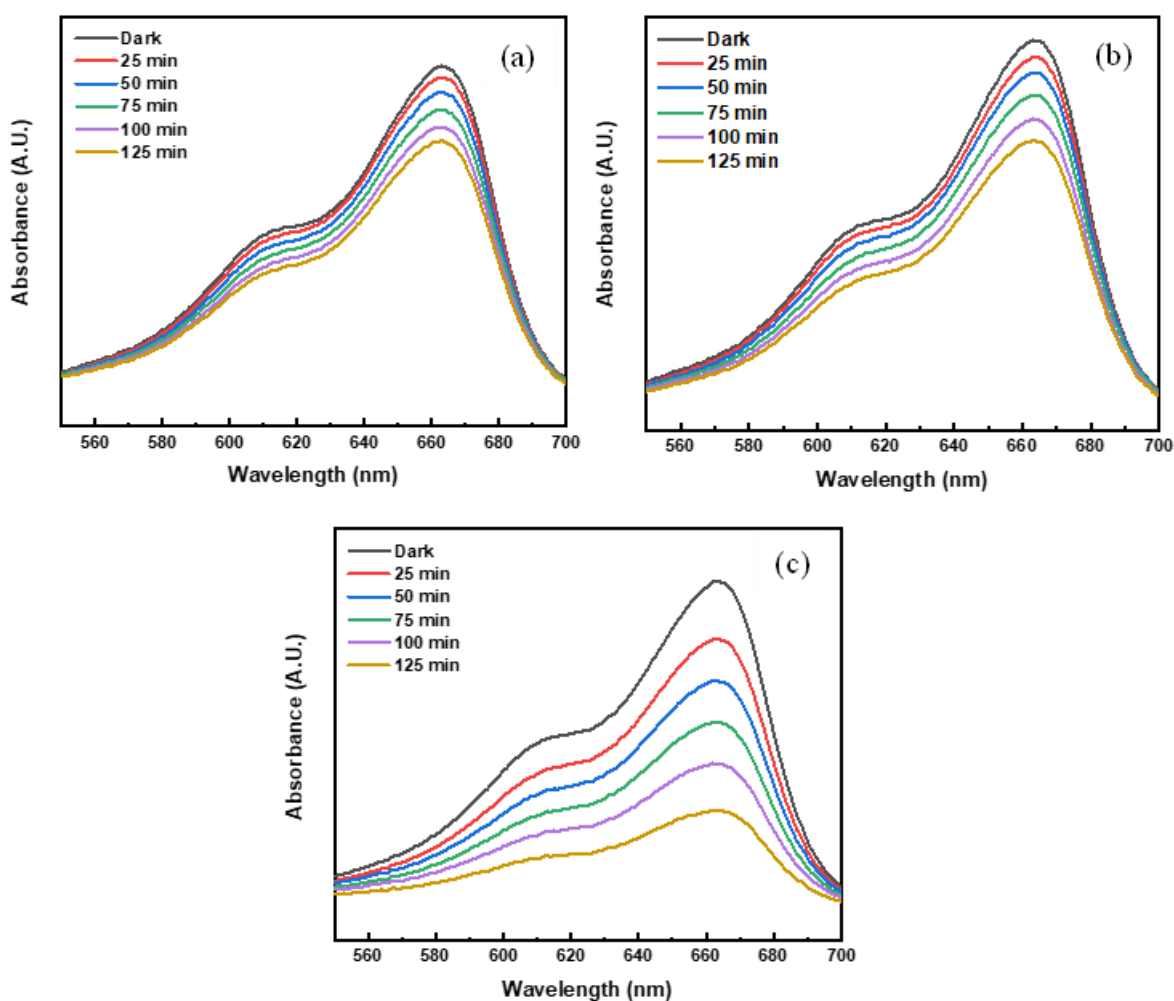


Figure 18. MB dye absorption spectra at several time intervals using Fe_2O_3 sample (a), WS_2 sample (b), and the heterostructure sample $\text{WS}_2/\text{Fe}_2\text{O}_3$ (c).

From the absorption spectra represented in figure 18, it is clear that the heterostructure $\text{WS}_2/\text{Fe}_2\text{O}_3$ achieved the best and the most significant photocatalytic activity against MB dye. These results indicate that constructing a heterostructure of semiconducting nanomaterials is an efficient technology for enhancing the photocatalytic properties of a photocatalyst.

The concentration C of the dye solution used was calculated using the standard curve method. To compute the efficiency of degradation of the implemented photocatalysts, the following equation was applied (132):

$$\text{Dye degradation efficiency \%} = \frac{C_0 - C}{C_0} * 100 \quad (4)$$

Where C_0 is the starting concentration of the dye solution and C is the concentration of the dye at a certain time t of relative exposure to irradiation. On the other hand, Langmuir-Hinshelwood model was implemented to obtain the reaction rates of MB dye degradation via the equation of pseudo-first-order kinetics (132):

$$\ln\left(\frac{C_0}{C}\right) = kt \quad (5)$$

Where k is the constant of reaction rate, which is the slope of the straight line resulting from the relationship between $\ln\left(\frac{C_0}{C}\right)$ and the time t .

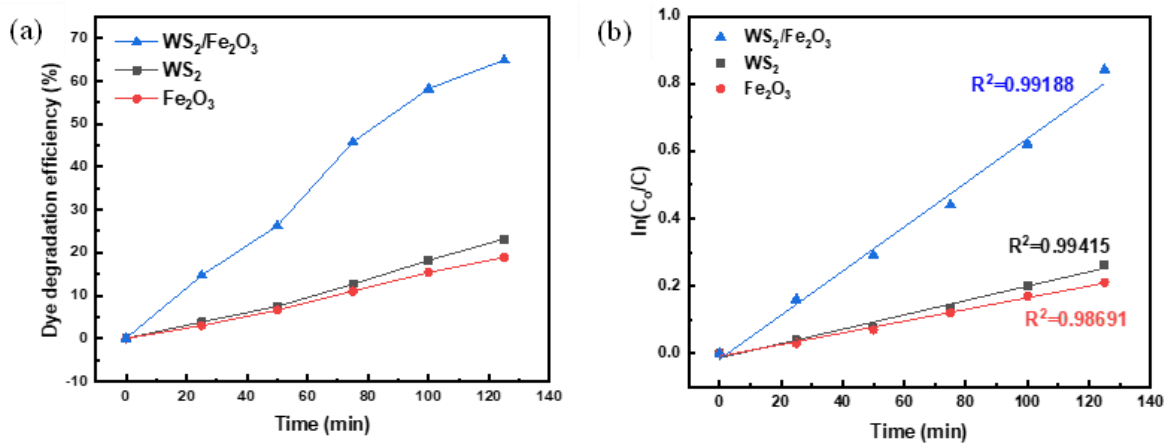


Figure 19. Photodegradation efficiency plots (a) and the kinetics plots (b) of the as-prepared photocatalysts.

Indeed, figure 19a emphasizes the enhancement performed by the heterostructure as the dye degradation efficiency reached as high as 64.9% whereas it did not exceed 18.9% and 23.1% for bare Fe₂O₃ and WS₂ respectively. In another words, the prepared heterostructure accomplished 3.4 and 2.8 times better photodegradation efficiency than that of each component alone, respectively. In

addition, the first-order kinetics were plotted for the three samples and the rate constant k values were calculated as follows 0.00174 min^{-1} for Fe_2O_3 , 0.00213 min^{-1} for WS_2 , and 0.00655 min^{-1} for $\text{WS}_2/\text{Fe}_2\text{O}_3$ as represented by figure 18b.

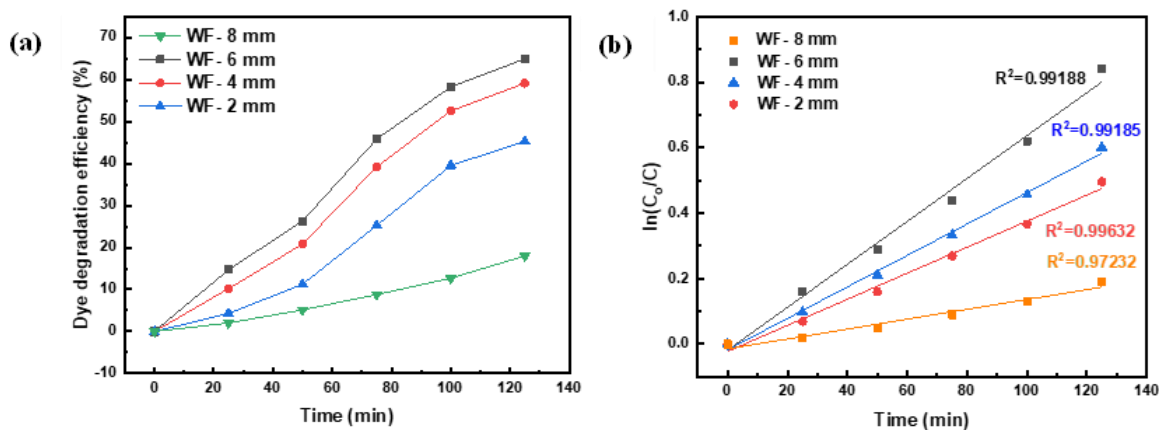


Figure 20. Dye degradation efficiency (a) and kinetic plots (b) of the as-prepared $\text{WS}_2/\text{Fe}_2\text{O}_3$ heterostructures grown at different heights.

Figure 20a represents the dye degradation curves obtained for the produced $\text{WS}_2/\text{Fe}_2\text{O}_3$ heterostructures. It can be observed that as the height increases from 2 to 4 mm, the photodegradation efficiency of the prepared samples increases, with a maximum photocatalytic activity of 64.9% at 6 mm height then it decreases significantly for the 8-mm sample. This can be accredited to the larger surface area of the small vertically aligned flakes of WS_2 distributed on Fe_2O_3 film in the 6 mm sample, whereas the 8 mm WF sample does not show WS_2 nanoflakes in the SEM images, which may affect the photocatalytic activity due to the incomplete growth of WS_2 nanoflakes. The photodegradation reaction was plotted as first-order linear expression as shown in figure 20b. All studied samples showed linear relationships between $\ln(C_0/C)$ and time that fit the first-order kinetics. For all samples, linear relationships were obtained between $\ln(C_0/C)$ and the irradiation time that follow the first-order kinetics. The values of the rate constant k for 2-, 4-, 6-, and 8-mm height samples were found as 0.00398 , 0.00480 , 0.00655 , and 0.00151 min^{-1} , respectively.

4.2.3. Proposed Photocatalytic Mechanism

Figure 21 illustrates the proposed mechanism of the photodegradation of MB dye solution using 6mm- WS₂/Fe₂O₃ heterostructure. When the heterostructure sample is immersed in the MB dye solution and gets exposed to solar irradiation, the photocatalyst absorbs this energy and the photoinduced charge carriers are generated. After that, the electron-hole pairs separate and migrate to the surface of the photocatalyst, where the MB molecules will be removed via redox reactions that produces free radicals including [∘]O₂⁻ and [∘]OH, which work as great oxidizing agents and decompose organic substances into H₂O and CO₂. In the case of this heterostructured photocatalysts, electrons transfer from the CB of WS₂ to the CB of Fe₂O₃. In contrast, holes transfer from the VB of Fe₂O₃ to the VB of WS₂. As a result, the recombination rate of the photogenerated charge carriers could be reduced prior to the exposure of visible light, which overcomes the challenge of the high recombination activity performed by bare Fe₂O₃. Accordingly, this heterostructure is able to generate more charge carriers with an improved separation and faster migration to the surface active sites leading to an enhanced photocatalytic performance in comparison with bare WS₂ and Fe₂O₃ (133,134).

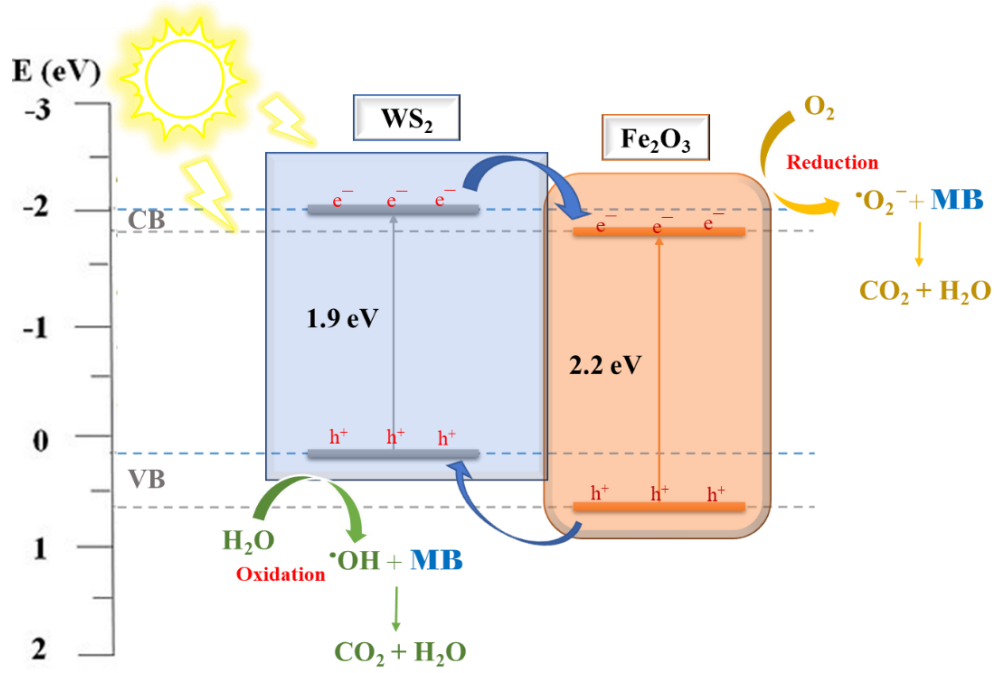


Figure 21. Schematic illustration of the proposed mechanism of MB dye photodegradation via the heterojunction WS₂/Fe₂O₃.

CHAPTER 5: CONCLUSION

To sum up, this study aimed to achieve an enhancement in the photocatalytic activity of α -Fe₂O₃ by preparing a heterostructure with a TMD material, WS₂. The synthesis of hematite NRs was accomplished using hydrothermal technique and two preparation conditions were investigated which are precursors' ratio and annealing temperature and their influence on the morphology of NRs was studied. First, it was noticed that increasing the amount of the additive sodium nitrate leads to hematite NRs that are more uniform in shape with an observed reduction in the holes formation. For the heterostructure construction, WS₂ nanoflakes was grown on the as-prepared hematite using CVD technique. The distance between the tungsten source and the Fe₂O₃ sample was found to affect the growth of WS₂ as well as the photocatalytic performance which was examined against MB dye solution under solar simulator irradiation. The best photodegradation activity was obtained by the heterostructure prepared at 6 mm high with a degradation percentage of 64.9%, which is 3.4 and 2.8 times better than bare Fe₂O₃ and WS₂, respectively.

FUTURE PRESPECTIVE

In the future, further investigation of the photocatalytic properties used in water treatment applications of hematite heterostructures can be accomplished, especially with TMDs nanostructures. For this sake, CVD could be a promising synthesis technique of a TMD, with studying the effect of different growth conditions such as quantities, pressure, and temperature, in addition to the substrate used for the heterostructure growth. Furthermore, some kinetic studies can be performed during the photodegradation experiments, as well as changing the sun light intensity with studying its effects. According to the fact that this photodegradation process results in producing carbon dioxide in the aqueous solution, the total organic carbon (TOC) test can be implemented to investigate the organic content of water after the dye degradation. Also, researchers can use other TMD material for the formation of Fe₂O₃ heterostructures.

REFERENCES

1. Jing L, Zhou W, Tian G, Fu H. Surface tuning for oxide-based nanomaterials as

- efficient photocatalysts. *Chem Soc Rev* [Internet]. 2013;42(24):9509–49. Available from: <http://dx.doi.org/10.1039/C3CS60176E>
2. Alharbi NS, Hu B, Hayat T, Rabah SO, Alsaedi A, Zhuang L, et al. Efficient elimination of environmental pollutants through sorption-reduction and photocatalytic degradation using nanomaterials. *Front Chem Sci Eng* [Internet]. 2020 [cited 2021 Dec 16];14(6):1124–35. Available from: <https://doi.org/10.1007/s11705-020-1923-z>
 3. Garg A, Singhanian T, Singh A, Sharma S, Rani S, Neogy A, et al. Photocatalytic Degradation of Bisphenol-A using N, Co Codoped TiO₂ Catalyst under Solar Light. *Sci Rep* [Internet]. 2019;9(1):1–13. Available from: <http://dx.doi.org/10.1038/s41598-018-38358-w>
 4. Jusoh NWC, Jalil AA, Triwahyono S, Setiabudi HD, Sapawe N, Satar MAH, et al. Sequential desilication–isomorphous substitution route to prepare mesostructured silica nanoparticles loaded with ZnO and their photocatalytic activity. *Appl Catal A Gen* [Internet]. 2013 Nov;468:276–87. Available from: <https://linkinghub.elsevier.com/retrieve/pii/S0926860X13005474>
 5. Ahmad M, Chen S, Ye F, Quan X, Afzal S, Yu H, et al. Efficient photo-Fenton activity in mesoporous MIL-100(Fe) decorated with ZnO nanosphere for pollutants degradation. *Appl Catal B Environ*. 2019 May 15;245:428–38.
 6. Fu L, Wu C, Zhou Y, Zuo J, Song G, Tan Y. Ozonation reactivity characteristics of dissolved organic matter in secondary petrochemical wastewater by single ozone, ozone/H₂O₂, and ozone/catalyst. *Chemosphere*. 2019 Oct 1;233:34–43.
 7. Lee CM, Palaniandy P, Dahlan I. Pharmaceutical residues in aquatic environment and water remediation by TiO₂ heterogeneous photocatalysis: a review. *Environ Earth Sci* [Internet]. 2017 Sep 1;76(17):611. Available from: <http://link.springer.com/10.1007/s12665-017-6924-y>

8. Ye S, Yan M, Tan X, Liang J, Zeng G, Wu H, et al. Facile assembled biochar-based nanocomposite with improved graphitization for efficient photocatalytic activity driven by visible light. *Appl Catal B Environ* [Internet]. 2019 Aug;250:78–88. Available from: <https://linkinghub.elsevier.com/retrieve/pii/S092633731930205X>
9. Fujishima A, Rao TN, Tryk DA. Titanium dioxide photocatalysis. *J Photochem Photobiol C Photochem Rev* [Internet]. 2000 Jun;1(1):1–21. Available from: <https://linkinghub.elsevier.com/retrieve/pii/S1389556700000022>
10. Ohtani B. Revisiting the fundamental physical chemistry in heterogeneous photocatalysis: Its thermodynamics and kinetics [Internet]. Vol. 16, *Physical Chemistry Chemical Physics*. The Royal Society of Chemistry; 2014 [cited 2022 Aug 20]. p. 1788–97. Available from: <https://pubs.rsc.org/en/content/articlehtml/2014/cp/c3cp53653j>
11. Kozlova EA, Parmon VN. Heterogeneous semiconductor photocatalysts for hydrogen production from aqueous solutions of electron donors. *Russ Chem Rev* [Internet]. 2017 Sep 30 [cited 2022 Aug 20];86(9):870–906. Available from: <https://iopscience.iop.org/article/10.1070/RCR4739>
12. Augugliaro V, Palmisano G, Palmisano L, Soria J. Heterogeneous photocatalysis and catalysis: An overview of their distinctive features. In: *Heterogeneous Photocatalysis: Relationships with Heterogeneous Catalysis and Perspectives*. Elsevier; 2019. p. 1–24.
13. Akerdi AG, Bahrami SH. Application of heterogeneous nano-semiconductors for photocatalytic advanced oxidation of organic compounds: A review. *J Environ Chem Eng* [Internet]. 2019 Oct;7(5):103283. Available from: <https://linkinghub.elsevier.com/retrieve/pii/S2213343719304063>
14. Maeda K, Teramura K, Lu D, Takata T, Saito N, Inoue Y, et al. Photocatalyst

- releasing hydrogen from water. *Nat* 2006 4407082 [Internet]. 2006 Mar 15 [cited 2022 Oct 3];440(7082):295–295. Available from: <https://www.nature.com/articles/440295a>
15. Kubacka A, Fernández-García M, Colón G. Advanced nanoarchitectures for solar photocatalytic applications. *Chem Rev*. 2012;112(3):1555–614.
 16. Osterloh FE. Inorganic materials as catalysts for photochemical splitting of water. *Chem Mater*. 2008;20(1):35–54.
 17. Qu Y, Duan X. Progress, challenge and perspective of heterogeneous photocatalysts. *Chem Soc Rev* [Internet]. 2013 Mar 11 [cited 2023 Mar 6];42(7):2568–80. Available from: <https://pubs.rsc.org/en/content/articlehtml/2013/cs/c2cs35355e>
 18. Alakhras F, Alhajri E, Haounati R, Ouachtak H, Addi AA, Saleh TA. A comparative study of photocatalytic degradation of Rhodamine B using natural-based zeolite composites. *Surfaces and Interfaces*. 2020 Sep 1;20:100611.
 19. Guo S, Zhang H, Chen Y, Liu Z, Yu B, Zhao Y, et al. Visible-Light-Driven Photoreduction of CO₂ to CH₄ over N,O,P-Containing Covalent Organic Polymer Submicrospheres. *ACS Catal* [Internet]. 2018 May 4;8(5):4576–81. Available from: <https://pubs.acs.org/doi/10.1021/acscatal.8b00989>
 20. Das S, Mahalingam H. Novel immobilized ternary photocatalytic polymer film based airlift reactor for efficient degradation of complex phthalocyanine dye wastewater. *J Hazard Mater* [Internet]. 2020 Feb;383:121219. Available from: <https://linkinghub.elsevier.com/retrieve/pii/S0304389419311732>
 21. Ashar A, Bhatti IA, Ashraf M, Tahir AA, Aziz H, Yousuf M, et al. Fe³⁺ @ ZnO/polyester based solar photocatalytic membrane reactor for abatement of RB5 dye. *J Clean Prod* [Internet]. 2020 Feb;246:119010. Available from: <https://linkinghub.elsevier.com/retrieve/pii/S0959652619338806>

22. Zhang L, Li X, Wang M, He Y, Chai L, Huang J, et al. Highly Flexible and Porous Nanoparticle-Loaded Films for Dye Removal by Graphene Oxide–Fungus Interaction. *ACS Appl Mater Interfaces* [Internet]. 2016 Dec 21;8(50):34638–47. Available from: <https://pubs.acs.org/doi/10.1021/acsami.6b10920>
23. Jorfi S, Pourfadakari S, Kakavandi B. A new approach in sono-photocatalytic degradation of recalcitrant textile wastewater using MgO@Zeolite nanostructure under UVA irradiation. *Chem Eng J* [Internet]. 2018 Jul;343:95–107. Available from: <https://linkinghub.elsevier.com/retrieve/pii/S1385894718302699>
24. Chowdhury A, Khan AA, Kumari S, Hussain S. Superadsorbent Ni–Co–S/SDS Nanocomposites for Ultrahigh Removal of Cationic, Anionic Organic Dyes and Toxic Metal Ions: Kinetics, Isotherm and Adsorption Mechanism. *ACS Sustain Chem Eng* [Internet]. 2019 Feb 18;7(4):4165–76. Available from: <https://pubs.acs.org/doi/10.1021/acssuschemeng.8b05775>
25. Kale G, Arbuji S, Chothe U, Khore S, Nikam L, Kale B. Highly Crystalline Ordered Cu-dopedTiO₂Nanostructure by Paper Templated Method: Hydrogen Production and Dye Degradation under Natural Sunlight. *J Compos Sci* [Internet]. 2020 May 4;4(2):48. Available from: <https://www.mdpi.com/2504-477X/4/2/48>
26. Wang L, Bahnemann DW, Bian L, Dong G, Zhao J, Wang C. Two-Dimensional Layered Zinc Silicate Nanosheets with Excellent Photocatalytic Performance for Organic Pollutant Degradation and CO₂ Conversion. *Angew Chemie Int Ed* [Internet]. 2019 Jun 11;58(24):8103–8. Available from: <https://onlinelibrary.wiley.com/doi/10.1002/anie.201903027>
27. Heidarpour H, Padervand M, Soltanieh M, Vossoughi M. Enhanced decolorization of rhodamine B solution through simultaneous photocatalysis and

- persulfate activation over Fe/C₃N₄ photocatalyst. Chem Eng Res Des [Internet]. 2020;153:709–20. Available from: <https://doi.org/10.1016/j.cherd.2019.09.007>
28. Padervand M. Visible-light photoactive Ag–AgBr/ α -Ag₃VO₄ nanostructures prepared in a water-soluble ionic liquid for degradation of wastewater. Appl Nanosci [Internet]. 2016 Nov 2;6(8):1119–26. Available from: <http://link.springer.com/10.1007/s13204-016-0525-z>
 29. Raza N, Raza W, Gul H, Azam M, Lee J, Vikrant K, et al. Solar-light-active silver phosphate/titanium dioxide/silica heterostructures for photocatalytic removal of organic dye. J Clean Prod [Internet]. 2020 May;254:120031. Available from: <https://linkinghub.elsevier.com/retrieve/pii/S0959652620300780>
 30. Demirci S, Yurddaskal M, Dikici T, Sarioğlu C. Fabrication and characterization of novel iodine doped hollow and mesoporous hematite (Fe₂O₃) particles derived from sol-gel method and their photocatalytic performances. J Hazard Mater [Internet]. 2018 Mar;345:27–37. Available from: <https://linkinghub.elsevier.com/retrieve/pii/S0304389417308312>
 31. Khodadadi B, Bordbar M, Nasrollahzadeh M. Green synthesis of Pd nanoparticles at Apricot kernel shell substrate using Salvia hydrangea extract: Catalytic activity for reduction of organic dyes. J Colloid Interface Sci [Internet]. 2017 Mar;490:1–10. Available from: <https://linkinghub.elsevier.com/retrieve/pii/S0021979716309092>
 32. Sudhaik A, Raizada P, Shandilya P, Jeong DY, Lim JH, Singh P. Review on fabrication of graphitic carbon nitride based efficient nanocomposites for photodegradation of aqueous phase organic pollutants. Vol. 67, Journal of Industrial and Engineering Chemistry. Elsevier; 2018. p. 28–51.
 33. Sharma S, Dutta V, Singh P, Raizada P, Rahmani-Sani A, Hosseini-

- Bandegharai A, et al. Carbon quantum dot supported semiconductor photocatalysts for efficient degradation of organic pollutants in water: A review. Vol. 228, *Journal of Cleaner Production*. Elsevier; 2019. p. 755–69.
34. Hasija V, Raizada P, Sudhaik A, Sharma K, Kumar A, Singh P, et al. Recent advances in noble metal free doped graphitic carbon nitride based nanohybrids for photocatalysis of organic contaminants in water: A review. Vol. 15, *Applied Materials Today*. Elsevier; 2019. p. 494–524.
35. Akter J, Hanif MA, Islam MA, Sapkota KP, Lee I, Hahn JR. Visible-light-active novel α -Fe₂O₃/Ta₃N₅ photocatalyst designed by band-edge tuning and interfacial charge transfer for effective treatment of hazardous pollutants. *J Environ Chem Eng* [Internet]. 2021 Dec;9(6):106831. Available from: <https://linkinghub.elsevier.com/retrieve/pii/S221334372101808X>
36. Book Reviews. Announcements. *Corros Rev* [Internet]. 1997 Dec;15(3–4):533–59. Available from: <https://www.degruyter.com/document/doi/10.1515/CORRREV.1997.15.3-4.533/html>
37. Wang C, Liu H, Sun Z. Heterogeneous Photo-Fenton Reaction Catalyzed by Nanosized Iron Oxides for Water Treatment. *Int J Photoenergy* [Internet]. 2012;2012:1–10. Available from: <http://www.hindawi.com/journals/ijp/2012/801694/>
38. Ohkoshi S, Namai A, Imoto K, Yoshikiyo M, Tarora W, Nakagawa K, et al. Nanometer-size hard magnetic ferrite exhibiting high optical-transparency and nonlinear optical-magnetoelectric effect. *Sci Rep* [Internet]. 2015 Oct 6;5(1):14414. Available from: <https://www.nature.com/articles/srep14414>
39. Mishra M, Chun D-M. α -Fe₂O₃ as a photocatalytic material: A review. *Appl Catal A Gen* [Internet]. 2015 Jun;498:126–41. Available from:

<https://linkinghub.elsevier.com/retrieve/pii/S0926860X15001878>

40. Chirita M, Grozescu I. Fe₂O₃ – Nanoparticles , Physical Properties and Their Photochemical And Photoelectrochemical Applications. Chem Bull Politeh Univ Timisoara. 2009;54(68):1–8.
41. Christoforidis KC, Montini T, Bontempi E, Zafeiratos S, Jaén JJD, Fornasiero P. Synthesis and photocatalytic application of visible-light active β -Fe₂O₃/g-C₃N₄ hybrid nanocomposites. Appl Catal B Environ. 2016 Jun 15;187:171–80.
42. Machala L, Tuček J, Zbořil R. Polymorphous Transformations of Nanometric Iron(III) Oxide: A Review. Chem Mater [Internet]. 2011 Jul 26;23(14):3255–72. Available from: <https://pubs.acs.org/doi/10.1021/cm200397g>
43. You J, Wang L, Zhao Y, Bao W. A review of amino-functionalized magnetic nanoparticles for water treatment: Features and prospects. J Clean Prod [Internet]. 2021 Jan;281:124668. Available from: <https://linkinghub.elsevier.com/retrieve/pii/S0959652620347120>
44. Chen C, Duan F, Zhao S, Wang W, Yang F, Nuansing W, et al. Porous Fe₂O₃ nanotubes with α - γ phase junction for enhanced charge separation and photocatalytic property produced by molecular layer deposition. Appl Catal B Environ [Internet]. 2019 Jul;248:218–25. Available from: <https://linkinghub.elsevier.com/retrieve/pii/S0926337319301407>
45. Pauling L, Hendricks SB. THE CRYSTAL STRUCTURES OF HEMATITE AND CORUNDUM. J Am Chem Soc [Internet]. 1925 Mar 1;47(3):781–90. Available from: <https://pubs.acs.org/doi/abs/10.1021/ja01680a027>
46. Darezereshki E. One-step synthesis of hematite (α -Fe₂O₃) nano-particles by direct thermal-decomposition of maghemite. Mater Lett [Internet]. 2011 Feb;65(4):642–5. Available from: <https://linkinghub.elsevier.com/retrieve/pii/S0167577X10009912>

47. Morales MP, Pecharroman C, Gonzalez Carreñ T, Serna CJ. Structural characteristics of uniform γ -Fe₂O₃ particles with different axial (length/width) ratios. *J Solid State Chem.* 1994 Jan 1;108(1):158–63.
48. Tuček J, Zbořil R, Namai A, Ohkoshi S. ϵ -Fe₂O₃ : An Advanced Nanomaterial Exhibiting Giant Coercive Field, Millimeter-Wave Ferromagnetic Resonance, and Magnetoelectric Coupling. *Chem Mater* [Internet]. 2010 Dec 28;22(24):6483–505. Available from: <https://pubs.acs.org/doi/10.1021/cm101967h>
49. MacHala L, Tuček J, Zbořil R. Polymorphous transformations of nanometric iron(III) oxide: A review. Vol. 23, *Chemistry of Materials*. American Chemical Society; 2011. p. 3255–72.
50. Shen S, Lindley SA, Chen X, Zhang JZ. Hematite heterostructures for photoelectrochemical water splitting: rational materials design and charge carrier dynamics. *Energy Environ Sci* [Internet]. 2016;9(9):2744–75. Available from: <http://xlink.rsc.org/?DOI=C6EE01845A>
51. Shen S. Toward efficient solar water splitting over hematite photoelectrodes. *J Mater Res* [Internet]. 2014 Jan 14;29(1):29–46. Available from: <http://link.springer.com/10.1557/jmr.2013.310>
52. Tang P, Arbiol J. Engineering surface states of hematite based photoanodes for boosting photoelectrochemical water splitting. *Nanoscale Horizons* [Internet]. 2019;4(6):1256–76. Available from: <http://xlink.rsc.org/?DOI=C9NH00368A>
53. Katselis G, Khamis MM, El-Aneed A, Willems JL, Low NH, Mohammed Saeid W, et al. Analysis of a series of chlorogenic acid isomers using differential ion mobility and tandem mass spectrometry. *Anal Chim Acta* [Internet]. 2016;933:164–74. Available from: <http://dx.doi.org/10.1016/j.aca.2016.05.041>
54. Xu C, Teja AS. Continuous hydrothermal synthesis of iron oxide and PVA-

- protected iron oxide nanoparticles. *J Supercrit Fluids* [Internet]. 2008 Feb;44(1):85–91. Available from: <https://linkinghub.elsevier.com/retrieve/pii/S0896844607003622>
55. Caremans TP, Kirschhock CEA, Verlooy P, Paul JS, Jacobs PA, Martens JA. Prototype high-throughput system for hydrothermal synthesis and X-ray diffraction of microporous and mesoporous materials. *Microporous Mesoporous Mater* [Internet]. 2006 Mar;90(1–3):62–8. Available from: <https://linkinghub.elsevier.com/retrieve/pii/S1387181105005846>
56. Blood PJ, Denyer JP, Azzopardi BJ, Poliakoff M, Lester E. A versatile flow visualisation technique for quantifying mixing in a binary system: application to continuous supercritical water hydrothermal synthesis (SWHS). *Chem Eng Sci* [Internet]. 2004 Jul;59(14):2853–61. Available from: <https://linkinghub.elsevier.com/retrieve/pii/S0009250904002404>
57. Wu K, Lian T. Quantum confined colloidal nanorod heterostructures for solar-to-fuel conversion. *Chem Soc Rev* [Internet]. 2016;45(14):3781–810. Available from: <http://xlink.rsc.org/?DOI=C5CS00472A>
58. Fauzi AA, Jalil AA, Mohamed M, Triwahyono S, Jusoh NWC, Rahman AFA, et al. Altering fiber density of cockscomb-like fibrous silica–titania catalysts for enhanced photodegradation of ibuprofen. *J Environ Manage* [Internet]. 2018 Dec;227:34–43. Available from: <https://linkinghub.elsevier.com/retrieve/pii/S0301479718309447>
59. Rosales M, Zoltan T, Yadarola C, Mosquera E, Gracia F, García A. The influence of the morphology of 1D TiO₂ nanostructures on photogeneration of reactive oxygen species and enhanced photocatalytic activity. *J Mol Liq* [Internet]. 2019 May;281:59–69. Available from: <https://linkinghub.elsevier.com/retrieve/pii/S0167732218362482>

60. Fu H, Sun S, Yang X, Li W, An X, Zhang H, et al. A facile coating method to construct uniform porous α -Fe₂O₃@TiO₂ core-shell nanostructures with enhanced solar light photocatalytic activity. Powder Technol [Internet]. 2018 Apr;328:389–96. Available from: <https://linkinghub.elsevier.com/retrieve/pii/S0032591018300809>
61. Zhou B, Li Y, Bai J, Li X, Li F, Liu L. Controlled synthesis of rh-In₂O₃ nanostructures with different morphologies for efficient photocatalytic degradation of oxytetracycline. Appl Surf Sci [Internet]. 2019 Jan;464:115–24. Available from: <https://linkinghub.elsevier.com/retrieve/pii/S0169433218321767>
62. Ahmed MG, Kandiel TA, Ahmed AY, Kretschmer I, Rashwan F, Bahnemann D. Enhanced Photoelectrochemical Water Oxidation on Nanostructured Hematite Photoanodes via p-CaFe₂O₄/n-Fe₂O₃ Heterojunction Formation. J Phys Chem C [Internet]. 2015 Mar 19;119(11):5864–71. Available from: <https://pubs.acs.org/doi/10.1021/jp512804p>
63. Tofanello A, Shen S, De Souza FL, Vayssieres L. Strategies to improve the photoelectrochemical performance of hematite nanorod-based photoanodes. APL Mater [Internet]. 2020;8(4). Available from: <https://doi.org/10.1063/5.0003146>
64. Qiu J, Yue C, Zheng W, Liu F, Zhu J. Enhanced photocatalytic degradation of sulfamethoxazole by stable hierarchical Fe₂O₃/Co₃O₄ heterojunction on nickel foam. Chinese Chem Lett [Internet]. 2021 Nov 1 [cited 2023 Jan 19];32(11):3431–4. Available from: <https://linkinghub.elsevier.com/retrieve/pii/S100184172100334X>
65. Zhang GY, Feng Y, Xu YY, Gao DZ, Sun YQ. Controlled synthesis of mesoporous α -Fe₂O₃ nanorods and visible light photocatalytic property. Mater

- Res Bull. 2012 Mar 1;47(3):625–30.
66. Maji SK, Mukherjee N, Mondal A, Adhikary B. Synthesis, characterization and photocatalytic activity of α -Fe₂O₃ nanoparticles. *Polyhedron*. 2012 Feb 9;33(1):145–9.
 67. Xu JS, Zhu YJ. α -Fe₂O₃ hierarchically hollow microspheres self-assembled with nanosheets: Surfactant-free solvothermal synthesis, magnetic and photocatalytic properties. *CrystEngComm* [Internet]. 2011 Jul 27 [cited 2023 Mar 9];13(16):5162–9. Available from: <https://pubs.rsc.org/en/content/articlehtml/2011/ce/c1ce05252g>
 68. Li M, Liu H, Pang S, Yan P, Liu M, Ding M, et al. Facile fabrication of three-dimensional fusiform-like α -Fe₂O₃ for enhanced photocatalytic performance. *Nanomaterials*. 2021;11(10).
 69. Lv R, Robinson JA, Schaak RE, Sun D, Sun Y, Mallouk TE, et al. Transition Metal Dichalcogenides and Beyond: Synthesis, Properties, and Applications of Single- and Few-Layer Nanosheets. *Acc Chem Res* [Internet]. 2015 Jan 20;48(1):56–64. Available from: <https://pubs.acs.org/doi/10.1021/ar5002846>
 70. Zeng Z, Yin Z, Huang X, Li H, He Q, Lu G, et al. Single-layer semiconducting nanosheets: High-yield preparation and device fabrication. *Angew Chemie - Int Ed* [Internet]. 2011 Nov 18 [cited 2022 May 9];50(47):11093–7. Available from: <https://pubmed.ncbi.nlm.nih.gov/22021163/>
 71. Zeng Z, Sun T, Zhu J, Huang X, Yin Z, Lu G, et al. An Effective Method for the Fabrication of Few-Layer-Thick Inorganic Nanosheets. *Angew Chemie Int Ed* [Internet]. 2012 Sep 3;51(36):9052–6. Available from: <https://onlinelibrary.wiley.com/doi/10.1002/anie.201204208>
 72. Lin Y-C, Dumcenco DO, Huang Y-S, Suenaga K. Atomic mechanism of the semiconducting-to-metallic phase transition in single-layered MoS₂. *Nat*

- Nanotechnol [Internet]. 2014 May 20;9(5):391–6. Available from: <http://www.nature.com/articles/nnano.2014.64>
73. Liu L, Kumar SB, Ouyang Y, Guo J. Performance Limits of Monolayer Transition Metal Dichalcogenide Transistors. *IEEE Trans Electron Devices*. 2011;58(9):3042–7.
 74. Al-Hilli AA, Evans BL. The preparation and properties of transition metal dichalcogenide single crystals. *J Cryst Growth*. 1972 Jul 1;15(2):93–101.
 75. Choi S, Kim C, Lee JY, Lee TH, Kwon KC, Kang S, et al. Vertically aligned MoS₂ thin film catalysts with Fe-Ni sulfide nanoparticles by one-step sulfurization for efficient solar water reduction. *Chem Eng J* [Internet]. 2021 Aug;418:129369. Available from: <https://linkinghub.elsevier.com/retrieve/pii/S1385894721009578>
 76. Le CT, Kim J, Ullah F, Nguyen AD, Nguyen Tran TN, Le T-E, et al. Effects of Interlayer Coupling and Band Offset on Second Harmonic Generation in Vertical MoS₂/MoS₂(1-x)Se_{2x} Structures. *ACS Nano* [Internet]. 2020 Apr 28;14(4):4366–73. Available from: <https://pubs.acs.org/doi/10.1021/acsnano.9b09901>
 77. Zhang J, Zhu Z, Feng X. Construction of Two-Dimensional MoS₂/CdS p-n Nanohybrids for Highly Efficient Photocatalytic Hydrogen Evolution. *Chem - A Eur J* [Internet]. 2014 Aug 18;20(34):10632–5. Available from: <https://onlinelibrary.wiley.com/doi/10.1002/chem.201402522>
 78. Zhu Y, Ling Q, Liu Y, Wang H, Zhu Y. Photocatalytic H₂ evolution on MoS₂-TiO₂ catalysts synthesized via mechanochemistry. *Phys Chem Chem Phys* [Internet]. 2015;17(2):933–40. Available from: <http://xlink.rsc.org/?DOI=C4CP04628E>
 79. Zhao W, Ghorannevis Z, Chu L, Toh M, Kloc C, Tan PH, et al. Evolution of

- electronic structure in atomically thin sheets of ws_2 and wse_2 . *ACS Nano* [Internet]. 2013 Jan 22 [cited 2023 Mar 18];7(1):791–7. Available from: <https://pubs.acs.org/doi/abs/10.1021/nn305275h>
80. Peimyoo N, Shang J, Cong C, Shen X, Wu X, Yeow EKL, et al. Nonblinking, intense two-dimensional light emitter: Monolayer WS_2 Triangles. *ACS Nano* [Internet]. 2013 Dec 23 [cited 2023 Mar 18];7(12):10985–94. Available from: <https://pubs.acs.org/doi/abs/10.1021/nn4046002>
 81. Kang J, Tongay S, Zhou J, Li J, Wu J. Band offsets and heterostructures of two-dimensional semiconductors. *Appl Phys Lett* [Internet]. 2013 Jan 9 [cited 2023 Mar 18];102(1):012111. Available from: <https://aip.scitation.org/doi/abs/10.1063/1.4774090>
 82. Voiry D, Yamaguchi H, Li J, Silva R, Alves DCB, Fujita T, et al. Enhanced catalytic activity in strained chemically exfoliated WS_2 nanosheets for hydrogen evolution. *Nat Mater* [Internet]. 2013 Jul 7 [cited 2023 Mar 18];12(9):850–5. Available from: <https://www.nature.com/articles/nmat3700>
 83. Sang Y, Zhao Z, Zhao M, Hao P, Leng Y, Liu H. From UV to near-infrared, WS_2 nanosheet: A novel photocatalyst for full solar light spectrum photodegradation. *Adv Mater* [Internet]. 2015 Jan 1 [cited 2023 Mar 18];27(2):363–9. Available from: <https://onlinelibrary.wiley.com/doi/full/10.1002/adma.201403264>
 84. Mahler B, Hoepfner V, Liao K, Ozin GA. Colloidal synthesis of 1T- WS_2 and 2H- WS_2 nanosheets: Applications for photocatalytic hydrogen evolution. *J Am Chem Soc* [Internet]. 2014 Oct 8 [cited 2023 Mar 18];136(40):14121–7. Available from: <https://pubs.acs.org/doi/abs/10.1021/ja506261t>
 85. Britnell L, Ribeiro RM, Eckmann A, Jalil R, Belle BD, Mishchenko A, et al. Strong light-matter interactions in heterostructures of atomically thin films.

- Science (80-) [Internet]. 2013 Jun 14 [cited 2023 Mar 18];340(6138):1311–4. Available from: <https://www.science.org/doi/10.1126/science.1235547>
86. Zhou J, Chen D, Bai L, Qin L, Sun X, Huang Y. Decoration of WS₂ as an effective noble-metal free cocatalyst on ZnIn₂S₄ for enhanced visible light photocatalytic hydrogen evolution. *Int J Hydrogen Energy*. 2018 Sep 27;43(39):18261–9.
 87. Jin Q, Dai X, Song J, Pu K, Wu X, An J, et al. High photocatalytic performance of g-C₃N₄/WS₂ heterojunction from first principles. *Chem Phys*. 2021 May 1;545:111141.
 88. Green MA. Thin-film solar cells: Review of materials, technologies and commercial status. *J Mater Sci Mater Electron*. 2007;18(SUPPL. 1):15–9.
 89. Bin Rafiq MKS, Amin N, Alharbi HF, Luqman M, Ayob A, Alharthi YS, et al. WS₂: A New Window Layer Material for Solar Cell Application. *Sci Rep*. 2020;10(1):1–11.
 90. Voiry D, Yamaguchi H, Li J, Silva R, Alves DCB, Fujita T, et al. Enhanced catalytic activity in strained chemically exfoliated WS₂ nanosheets for hydrogen evolution. *Nat Mater*. 2013;12(9):850–5.
 91. Nawaz A, Goudarzi S, Saravanan P, Zarrin H. Z-scheme induced g-C₃N₄/WS₂ heterojunction photocatalyst with improved electron mobility for enhanced solar photocatalysis. *Sol Energy* [Internet]. 2021;228(September):53–67. Available from: <https://doi.org/10.1016/j.solener.2021.09.040>
 92. Masoumi Z, Tayebi M, Lee BK. Ultrasonication-assisted liquid-phase exfoliation enhances photoelectrochemical performance in α -Fe₂O₃/MoS₂ photoanode. *Ultrason Sonochem* [Internet]. 2021;72:105403. Available from: <https://doi.org/10.1016/j.ultsonch.2020.105403>
 93. Behtaj Lejbini M, Sangpour P. Hydrothermal synthesis of α -Fe₂O₃-decorated

- MoS₂ nanosheets with enhanced photocatalytic activity. *Optik (Stuttg)* [Internet]. 2019 Jan;177:112–7. Available from: <https://linkinghub.elsevier.com/retrieve/pii/S0030402618313147>
94. Zhang Y, Chen P, Wen F, Meng Y, Yuan B, Wang H. Synthesis of S-rich flower-like Fe₂O₃-MoS₂ for Cr(VI) removal. *Sep Sci Technol* [Internet]. 2016 Jul 23;51(11):1779–86. Available from: <https://www.tandfonline.com/doi/full/10.1080/01496395.2016.1178285>
95. Alrobei H, Kumar A, Ram MK. A New Insight in the Physical and Photoelectrochemical Properties of Molybdenum Disulfide Alpha-Hematite Nanocomposite Films. *Am J Anal Chem* [Internet]. 2017;08(08):523–39. Available from: <http://www.scirp.org/journal/doi.aspx?DOI=10.4236/ajac.2017.88038>
96. Jia-nan Y, Shu W, Yong-xin J. Preparation of Fe₂O₃/WS₂ heterostructures with enhanced photocatalytic performances for dye degradation and Cr (VI) reduction. *Ferroelectrics* [Internet]. 2022 Jul 4;594(1):33–43. Available from: <https://www.tandfonline.com/doi/full/10.1080/00150193.2022.2078114>
97. Behera GC, Rani S, Khatun N, Rath JK, Roy SC. WS₂ nanosheets functionalized Fe₂O₃ nanorod arrays as a type II heterojunction for photoelectrochemical water splitting. *Appl Surf Sci Adv* [Internet]. 2022 Oct;11:100293. Available from: <https://linkinghub.elsevier.com/retrieve/pii/S2666523922000836>
98. Masoumi Z, Tayebi M, Kolaei M, Lee BK. Efficient and stable core-shell α-Fe₂O₃/WS₂/WO_x photoanode for oxygen evolution reaction to enhance photoelectrochemical water splitting. *Appl Catal B Environ*. 2022 Sep 15;313.
99. Sun D, Jia L, Wang C, Liu H, Chen R. Preparation of the additive-modified α-Fe₂O₃/g-C₃N₄ Z-scheme composites with improved visible-light photocatalytic activity. *J Environ Chem Eng* [Internet]. 2021 Oct;9(5):106274. Available from:

<https://linkinghub.elsevier.com/retrieve/pii/S2213343721012513>

100. Harijan DKL, Gupta S, Ben SK, Srivastava A, Singh J, Chandra V. High photocatalytic efficiency of α -Fe₂O₃ - ZnO composite using solar energy for methylene blue degradation. *Phys B Condens Matter* [Internet]. 2022 Feb;627:413567. Available from: <https://linkinghub.elsevier.com/retrieve/pii/S0921452621007201>
101. de la Rosa FM, Papac J, Garcia-Ballesteros S, Kovačić M, Katančić Z, Kušić H, et al. Solar Light Activation of Persulfate by TiO₂/Fe₂O₃ Layered Composite Films for Degradation of Amoxicillin: Degradation Mechanism, Matrix Effects, and Toxicity Assessments. *Adv Sustain Syst* [Internet]. 2021 Nov 1 [cited 2023 Jan 17];5(11):2100119. Available from: <https://onlinelibrary.wiley.com/doi/full/10.1002/adsu.202100119>
102. Choquehuanca A, Ruiz-Montoya JG, La Rosa-Toro Gómez A. Discoloration of methylene blue at neutral pH by heterogeneous photo-Fenton-like reactions using crystalline and amorphous iron oxides. *Open Chem* [Internet]. 2021 Jan 1 [cited 2023 Jun 6];19(1):1009–20. Available from: <https://www.degruyter.com/document/doi/10.1515/chem-2021-0077/html>
103. Teng X, Li J, Wang Z, Wei Z, Chen C, Du K, et al. Performance and mechanism of methylene blue degradation by an electrochemical process. *RSC Adv* [Internet]. 2020 Jun 29 [cited 2023 Jun 6];10(41):24712–20. Available from: <https://pubs.rsc.org/en/content/articlehtml/2020/ra/d0ra03963b>
104. Rahmaninezhad SA, Mehrdadi N, Mahzari Z. Analysis of the factors controlling the performance of a photoelectrocatalytic cell separated by UF membrane in degrading methylene blue. *J Aust Ceram Soc* [Internet]. 2021 Feb 1 [cited 2023 Jun 6];57(1):163–72. Available from: <https://link.springer.com/article/10.1007/s41779-020-00518-5>

105. Nasar A, Mashkoo F. Application of polyaniline-based adsorbents for dye removal from water and wastewater—a review [Internet]. Vol. 26, *Environmental Science and Pollution Research*. Springer; 2019 [cited 2023 Jun 6]. p. 5333–56. Available from: <https://link.springer.com/article/10.1007/s11356-018-3990-y>
106. Gan YX, Jayatissa AH, Yu Z, Chen X, Li M. Hydrothermal Synthesis of Nanomaterials [Internet]. Vol. 2020, *Journal of Nanomaterials*. Hindawi; 2020 [cited 2023 Feb 25]. Available from: <https://www.hindawi.com/journals/jnm/2020/8917013/>
107. Mirzaei A, Neri G. Microwave-assisted synthesis of metal oxide nanostructures for gas sensing application: A review. *Sensors Actuators B Chem* [Internet]. 2016 Dec;237:749–75. Available from: <https://linkinghub.elsevier.com/retrieve/pii/S0925400516309674>
108. Yang G, Park S-J. Conventional and Microwave Hydrothermal Synthesis and Application of Functional Materials: A Review. *Materials (Basel)* [Internet]. 2019 Apr 11;12(7):1177. Available from: <https://www.mdpi.com/1996-1944/12/7/1177>
109. Nandagudi A, Nagarajarao SH, Santosh MS, Basavaraja BM, Malode SJ, Mascarenhas RJ, et al. Hydrothermal synthesis of transition metal oxides, transition metal oxide/carbonaceous material nanocomposites for supercapacitor applications. Vol. 19, *Materials Today Sustainability*. Elsevier; 2022. p. 100214.
110. Zhang H. Ultrathin Two-Dimensional Nanomaterials. *ACS Nano* [Internet]. 2015 Oct 27;9(10):9451–69. Available from: <https://pubs.acs.org/doi/10.1021/acsnano.5b05040>
111. Lee Y-H, Zhang X-Q, Zhang W, Chang M-T, Lin C-T, Chang K-D, et al. Synthesis of Large-Area MoS₂ Atomic Layers with Chemical Vapor

- Deposition. *Adv Mater* [Internet]. 2012 May 2;24(17):2320–5. Available from: <https://onlinelibrary.wiley.com/doi/10.1002/adma.201104798>
112. Shi Y, Li H, Li L-J. Recent advances in controlled synthesis of two-dimensional transition metal dichalcogenides via vapour deposition techniques. *Chem Soc Rev* [Internet]. 2015 Apr 28 [cited 2023 Feb 27];44(9):2744–56. Available from: <https://pubs.rsc.org/en/content/articlehtml/2015/cs/c4cs00256c>
113. Ji Q, Zhang Y, Zhang Y, Liu Z. Chemical vapour deposition of group-VIB metal dichalcogenide monolayers: engineered substrates from amorphous to single crystalline. *Chem Soc Rev* [Internet]. 2015 Apr 28 [cited 2023 Feb 27];44(9):2587–602. Available from: <https://pubs.rsc.org/en/content/articlehtml/2015/cs/c4cs00258j>
114. Wang S, Rong Y, Fan Y, Pacios M, Bhaskaran H, He K, et al. Shape evolution of monolayer MoS₂ crystals grown by chemical vapor deposition. *Chem Mater* [Internet]. 2014 Nov 25 [cited 2023 Feb 27];26(22):6371–9. Available from: <https://pubs.acs.org/doi/full/10.1021/cm5025662>
115. Zhang Y, Zhang Y, Ji Q, Ju J, Yuan H, Shi J, et al. Controlled Growth of High-Quality Monolayer WS₂ Layers on Sapphire and Imaging Its Grain Boundary. *ACS Nano* [Internet]. 2013 Oct 22 [cited 2023 Feb 27];7(10):8963–71. Available from: <https://pubs.acs.org/doi/full/10.1021/nn403454e>
116. Chen J, Liu B, Liu Y, Tang W, Tai Nai C, Li L, et al. Chemical Vapor Deposition of Large-Sized Hexagonal WSe₂ Crystals on Dielectric Substrates. *Adv Mater* [Internet]. 2015 Nov 1 [cited 2023 Feb 27];27(42):6722–7. Available from: <https://onlinelibrary.wiley.com/doi/full/10.1002/adma.201503446>
117. Methods for Assessing Surface Cleanliness. In: *Developments in Surface Contamination and Cleaning, Volume 12*. Elsevier; 2019. p. 23–105.
118. X-Ray diffraction (XRD) :: Anton Paar Wiki [Internet]. [cited 2021 Oct 26].

Available from: <https://wiki.anton-paar.com/en/x-ray-diffraction-xrd/>

119. XRD Basics [Internet]. [cited 2021 Oct 26]. Available from: <https://www.physics.upenn.edu/~heiney/datasqueeze/basics.html>
120. Raman C V., Krishnan KS. A powerful tool for material identification: Raman spectroscopy. *Nature* [Internet]. 1928 [cited 2023 Mar 1];121(3048):501–2. Available from: <https://www.nature.com/articles/121501c0>
121. Li YS, Church JS. Raman spectroscopy in the analysis of food and pharmaceutical nanomaterials. Vol. 22, *Journal of Food and Drug Analysis*. No longer published by Elsevier; 2014. p. 29–48.
122. Vašková H. INTERNATIONAL JOURNAL OF MATHEMATICAL MODELS AND METHODS IN APPLIED SCIENCES A powerful tool for material identification : Raman spectroscopy. *Int J Math Model Methods Applied Sci*. 2011;5(7):1205–12.
123. Vernon-Parry KD. Scanning electron microscopy: an introduction. *III-Vs Rev* [Internet]. 2000 Jul;13(4):40–4. Available from: <https://linkinghub.elsevier.com/retrieve/pii/S096112900080006X>
124. van der Heide P. *X-Ray Photoelectron Spectroscopy* [Internet]. Wiley; 2011. Available from: <https://onlinelibrary.wiley.com/doi/book/10.1002/9781118162897>
125. Chamritski I, Burns G. Infrared- and Raman-Active Phonons of Magnetite, Maghemite, and Hematite: A Computer Simulation and Spectroscopic Study. *J Phys Chem B* [Internet]. 2005 Mar 1;109(11):4965–8. Available from: <https://pubs.acs.org/doi/10.1021/jp048748h>
126. Vayssieres L, Beermann N, Lindquist S-E, Hagfeldt A. Controlled Aqueous Chemical Growth of Oriented Three-Dimensional Crystalline Nanorod Arrays: Application to Iron(III) Oxides. *Chem Mater* [Internet]. 2001 Feb 1;13(2):233–

5. Available from: <https://pubs.acs.org/doi/10.1021/cm001202x>
127. Liu Q, Chen C, Yuan G, Huang X, Lü X, Cao Y, et al. Morphology-controlled α -Fe₂O₃ nanostructures on FTO substrates for photoelectrochemical water oxidation. *J Alloys Compd* [Internet]. 2017;715:230–6. Available from: <http://dx.doi.org/10.1016/j.jallcom.2017.04.213>
128. Zong X, Han J, Ma G, Yan H, Wu G, Li C. Photocatalytic H₂ Evolution on CdS Loaded with WS₂ as Cocatalyst under Visible Light Irradiation. *J Phys Chem C* [Internet]. 2011 Jun 23;115(24):12202–8. Available from: <https://pubs.acs.org/doi/10.1021/jp2006777>
129. Akple MS, Low J, Wageh S, Al-Ghamdi AA, Yu J, Zhang J. Enhanced visible light photocatalytic H₂-production of g-C₃N₄/WS₂ composite heterostructures. *Appl Surf Sci* [Internet]. 2015 Dec;358:196–203. Available from: <https://linkinghub.elsevier.com/retrieve/pii/S0169433215020747>
130. Yamashita T, Hayes P. Analysis of XPS spectra of Fe²⁺ and Fe³⁺ ions in oxide materials. *Appl Surf Sci* [Internet]. 2008 Feb;254(8):2441–9. Available from: <https://linkinghub.elsevier.com/retrieve/pii/S0169433207013748>
131. Ma L, Xu J, Liu Z, Liu Y, Liu X, Xu S. Fe₂O₃ hexagonal nanosheets assembled with NiS formed p–n heterojunction for efficient photocatalytic hydrogen evolution. *J Mater Sci* [Internet]. 2022 Mar 15;57(12):6734–48. Available from: <https://link.springer.com/10.1007/s10853-022-07064-4>
132. Sabarinathan M, Harish S, Archana J, Navaneethan M, Ikeda H, Hayakawa Y. Controlled exfoliation of monodispersed MoS₂ layered nanostructures by a ligand-assisted hydrothermal approach for the realization of ultrafast degradation of an organic pollutant. *RSC Adv* [Internet]. 2016;6(111):109495–505. Available from: <http://xlink.rsc.org/?DOI=C6RA24355J>
133. Chen L, Huang C-P, Chuang Y, Nguyen T-B, Chen C-W, Dong C-D. Z -Scheme

MoS₂/TiO₂/graphene nanohybrid photocatalysts for visible light-induced degradation for highly efficient water disinfection and antibacterial activity. *New J Chem* [Internet]. 2022;46(29):14159–69. Available from: <http://xlink.rsc.org/?DOI=D2NJ01824A>

134. Pandey SK, Mishra PK, Tiwary D. Enhanced photocatalytic performance of NiS/ZnO nanocomposite for the remediation of PNP and RhB dye. *J Environ Chem Eng* [Internet]. 2022 Jun;10(3):107459. Available from: <https://linkinghub.elsevier.com/retrieve/pii/S2213343722003323>